Corrosion Science 214 (2023) 111031

Contents lists available at ScienceDirect

Corrosion Science

journal homepage: www.elsevier.com/locate/corsci

Role of cementite morphology on corrosion layer formation of high-strength carbon steels in sweet and sour environments

Shabnam Karimi [a,*], Iman Taji [a], Tarlan Hajilou [a], Simona Palencsár [b], Arne Dugstad [b], Afrooz Barnoush [a,c], Kim Verbeken [d], Tom Depover [d], Roy Johnsen [a]

[a] Department of Mechanical and Industrial Engineering, Norwegian University of Science and Technology (NTNU), N-7491 Trondheim, Norway
[b] Institute for Energy Technology (IFE), P.O. Box 40, NO-2027, Kjeller, Norway
[c] Qatar Environment and Energy Research Institute (QEERI), Hamad Bin Khalifa University (HBKU), P.O. Box 34110, Doha, Qatar
[d] Department of Materials, Textiles and Chemical Engineering, Ghent University (UGent), Technologiepark 46, B-9052 Ghent, Belgium

ARTICLE INFO

Keywords:
Cementite morphology
Ferritic/pearlitic microstructure
Carbon steel corrosion
CO_2 environment
CO_2/H_2S environment

ABSTRACT

The effect of cementite morphology on the corrosion layer formation of four high-strength carbon steels was studied in an aqueous solution containing CO_2 and CO_2/H_2S. The linear polarization resistance and weight loss data reveal that as the cementite phase fraction is increased, the corrosion rate increases in CO_2 environment, while no trend is observed in the CO_2/H_2S environment. The results indicate that a porous and, non protective corrosion layer forms in the CO_2 environment, whereas a protective layer forms in the CO_2/H_2S environment. A mechanism that explains the role of cementite morphology on corrosion layer formation in a CO_2 environment is proposed for the studied materials.

1. Introduction

In the oil and gas industry, carbon steels are the most commonly used materials for pipe lines because of their excellent mechanical properties, availability, and cost. In a flexible pipe used as a riser, the armor wires are an integrated part of the multi-layer structure of the pipe, bearing the weight of the entire pipe [1]. Armor wires are typically made of high-strength carbon steels to sustain tensile loads owing to high tension and dynamic motions on flexible pipes [2,3]. Carbon steel used in the oil and gas industry experiences severe environmental conditions owing to the presence of corrosive elements and reactions that produce hydrogen in the environment. CO_2 and H_2S contained in gas and oil dissolve in water, produce H^+ ions, and lower the pH accordingly to create an acidic environment [4,5]:

$$CO_2 + H_2O \rightleftarrows H_2CO_3 \quad (1)$$

$$H_2CO_3 \rightleftarrows H^+ + HCO_3^- \quad (2)$$

$$HCO_3^- \rightleftarrows H^+ + CO_3^{2-} \quad (3)$$

$$H_2S \rightleftarrows H^+ + HS^- \quad (4)$$

$$HS^- \rightleftarrows H^+ + S^{2-} \quad (5)$$

The ions (HCO_3^-, CO_3^{2-}, HS^-, S^{2-}) can react with the released Fe^{2+} ions and control the corrosion process through the formation of an iron carbonate ($FeCO_3$) layer in a CO_2 environment and an iron sulfide layer in a H_2S environment [6,7]:

$$Fe^{2+} + 2HCO_3^- \rightleftarrows Fe(HCO_3)_2 \quad (6)$$

$$Fe(HCO_3)_2 \rightleftarrows FeCO_3 + CO_2 + H_2O \quad (7)$$

$$Fe^{2+} + CO_3^{2-} \rightleftarrows FeCO_3 \quad (8)$$

$$FeHS^+ \rightleftarrows FeS_{1-x} + xHS^- + (1-x)H^+ \quad (9)$$

$$Fe^{2+} + S^{2-} \rightleftarrows FeS \quad (10)$$

In the coexistence system of CO_2/H_2S, the corrosion layers that formed on the carbon steel surface are more complex. The environmental effects on the corrosion layer formation in a CO_2/H_2S environment have been extensively investigated, such as the effect of the H_2S partial pressure on corrosion layer [8–15], the effect of fluid flow on corrosion layer formation and dissolution [16,17], the dependence of corrosion product formation and morphology on the pH [18–20], the role of temperature on the corrosion products [21–24], and the relation between the corrosion layer and solution chemistry [25–27].

* Corresponding author.
E-mail address: shabnam.karimi@ntnu.no (S. Karimi).

https://doi.org/10.1016/j.corsci.2023.111031
Received 6 September 2022; Received in revised form 1 February 2023; Accepted 6 February 2023
Available online 9 February 2023
0010-938X/© 2023 The Author(s). Published by Elsevier Ltd. This is an open access article under the CC BY license (http://creativecommons.org/licenses/by/4.0/).

The corrosion rate of pipe line steels in a CO_2/H_2S brine system significantly depends on the H_2S partial pressure that accelerates the formation of the protective iron sulfide layer and decreases the corrosion [11]. Wang et al. [8] investigated the effect of H_2S partial pressure on the corrosion products formed in high-strength sulfur-resistant steel in oilfield-produced water under supercritical CO_2 conditions. The results of their study indicated that the structure of the corrosion product evolved from monolayer to bilayer with an increase in the H_2S partial pressure. The inner layer of the bilayer consisted of iron sulfide and $FeCO_3$ and the outer layer was $FeCO_3$. The density of the corrosion layer increased with an increase in the H_2S partial pressure, which reduced steel corrosion. The CO_2/H_2S ratio in their study was greater than 1500. It has been reported elsewhere that no $FeCO_3$ were detected in the corrosion products formed at CO_2/H_2S ratios below 1500 [15]. Wang et al. [28] reported that in the presence of H_2S, the corrosion layer exhibited a three-layer structure in a corrosive environment. Because H_2S can prevent the formation of iron oxides, the middle and inner layers are enriched with iron sulfides and iron oxides, respectively, and the outer layer is composed of hydroxides. In another study, the competitive formation of $FeCO_3$ and FeS layers on $API\ X65$ steel exposed to sweet and sour environments was investigated. The results indicated that a protective corrosion layer formed at 120 °C regardless of the H_2S presence. In the absence of H_2S, a steady and dense $FeCO_3$ layer was formed. In the presence of H_2S, the formation of the FeS film decreased the CO_2 corrosion process and hindered the $FeCO_3$ precipitation. Hesketh et al. [9] suggested that in an aqueous CO_2/H_2S system at high H_2S partial pressures, a protective and, dense sulfide layer forms on the metal surface, which limits the steel dissolution and transport of H_2S on the surface of the metal and prevents pit development.

The other important environmental factor that can affect the corrosion product formation is pH. In general, the literature confirms that at high pH values, and in the presence of H_2S, iron sulfide can precipitate on the metal surface [20]. Sardisco et al. [18] studied the protectiveness of the corrosion layer formed on Armco iron in a $CO_2/H_2S/H_2O$ environment with pH values ranging from 3 to 11. They reported that the corrosion layer showed the least protection in the pH range of 6.5 to 8.

In a study by Abelev et al. [21], the effect of temperature and different H_2S concentrations on the corrosion layer formed on iron with exposure to the CO_2-saturated 3 wt% NaCl solution was investigated. The results revealed that a protective layer, including $Fe(II)$ bonded to O and S, forms with the addition of 5 ppm H_2S at ambient temperature. At high H_2S concentrations, a thick porous, and inhomogeneous corrosion layer is formed, which is less protective. At a high temperature, 85 °C with the addition of 50 ppm H_2S, a dense protective corrosion layer of FeS_2, $FeCO_3$, and Fe_3O_4, is formed. The temperature can also affect the structure of the iron sulfide product, which forms in the presence of H_2S. Shi et al. [22] argued that the formation of mackinawite on $X60$ steel occurs at low temperatures and H_2S partial pressures, whereas pyrrhotite forms at high temperatures and H_2S partial pressures.

As reported in the literature, fluid flow prevents the formation of a protective scale [17]. Zhang et al. [16] studied the synergistic effects of fluid flow, CO_2, and H_2S on the corrosion layer formation on low-carbon steel. They concluded that in the absence of H_2S, the fluid flow can facilitate the transport of Fe^{2+} ions and decrease Fe^{2+} concentration between the Fe_3C remaining layers. Therefore, the formation of a porous and loose corrosion layer occurs that can easily break in some regions under the action of fluid flow. In the presence of H_2S, the $FeCO_3$ formation can be prevented by preferential adsorption of $FeHS^+$ ions, which forms an iron sulfide film.

In addition to the environmental conditions, carbon steel alloying elements [29–31] and microstructure influence the corrosion behavior and the corrosion layer formation. Palacios et al. [32] identified that under CO_2 exposure in an aqueous environment, the adherence of the corrosion layer to the steel as well as the thickness of the layer are influenced by the microstructure of the steel. They revealed that the $FeCO_3$ layer formed on the normalized specimen was thicker and better attached to steel than the quenched and tempered specimen layers. They explained that the $FeCO_3$ formation on a normalized specimen with a pearlitic microstructure was dependent on the remaining cementite distribution. As the iron between the cementite layers corroded away, a cementite phase was left behind with cavities between the cementite layers, and the local concentration of Fe^{2+} ions increased in these cavities. Local flow stagnation and high Fe^{2+} concentrations in the cavities allowed the formation of $FeCO_3$ between the remaining cementite layers. Dugstad et al. [33] discussed the effect of various heat treatments on corrosion layer formation in chromium-containing and unalloyed steels in a CO_2 environment. In unalloyed steels, they found that the adherence of the protective corrosion layer decreased with increasing tempering temperature, while a protective corrosion layer formed on the chromium-containing steels, and no mesa attack was observed regardless of their heat treatment. Kim et al. [34] reported iron sulfide layer precipitation on steel to be significantly dependent on the steel microstructure and cementite distribution. They mentioned that differences in the shape and distribution of the cementite phase can influence the mechanical attachment of the iron sulfide layer to the steel. Lopez et al. [35] discussed the effect of the steel microstructure on the corrosion layer properties, such as morphology and different chemical compound proportions. Ueda et al. [36] proposed that the lamellar morphology of cementite promotes more efficient adherence of the corrosion products to the steel substrate. This correlation between the lamellar cementite and corrosion layer adherence has also been presented in other studies [37,38]. According to Anyanwu et al. [37], the presence of cementite promotes the precipitation of iron sulfide in the pearlite regions in an H_2S environment. In general, the favored precipitation of iron sulfide in the pearlite areas of ferritic/pearlitic steel has been previously reported [39,40].

Considering the substantial investigation of the environmental factors affecting the corrosion rate (CR) and corrosion layer, the corrosion behavior in CO_2 and CO_2/H_2S environments requires detailed investigation on the effects of the microstructure of carbon steels. The environmental effects coupled with the role of carbon steel microstructure on corrosion allow for a more elaborate understanding of the corrosion of carbon steels in CO_2 and CO_2/H_2S environments.

Most studies that investigated the role of the microstructure or cementite morphology on the corrosion behavior of steels have been conducted on low or medium carbon steels, and they have generally compared different microstructures such as pearlites with martensites, or bainites. Moreover, few studies have focused on the effect of cementite morphology on corrosion layer formation. The present study investigated the effects of cementite morphology on the corrosion behavior and corrosion layer formation of three high-carbon steels and one low-carbon steel, which are all applied as tensile armor wires. The carbon steel microstructures included ferrite/pearlite and spheroidite, and they have delicate differences. Therefore, detailed microstructural characterizations were conducted to reveal the role of cementite morphology on corrosion layer formation in both CO_2 and CO_2/H_2S environments.

2. Experimental

2.1. Materials and sample preparation

Four carbon steels with different carbon contents and microstructures are investigated in this study. Carbon steels are tensile armor wires of flexible pipes, received in the form of drawn curved wires with widths of 9 to 12 mm and a thickness of 3 mm. Their chemical compositions and mechanical properties [41,42] are summarized in Table 1.

Table 1
Chemical composition and the mechanical properties (yield strength, YS, and ultimate tensile strength, UTS) of the studied materials [41].

Material (wt%)	C	Al	Si	P	Mo	V	Cr	Mn	Ni	Cu	YS (GPa)	UTS (GPa)
$CS28$	0.28	0.32	0.32	0.20	0.20	0.40	0.42	0.72	0.46	0.62	0.8	0.85
$CS62$	0.62	0.26	0.40	0.23	0.46	0.70	0.61	1.36	0.89	0.75	1.1	1.3
$CS65$	0.65	0.30	0.24	0.20	0.35	0.51	0.51	0.96	0.60	0.75	1.25	1.4
$CS83$	0.83	0.19	0.35	0.30	0.35	0.54	0.55	1.07	0.69	0.59	1.4	1.6

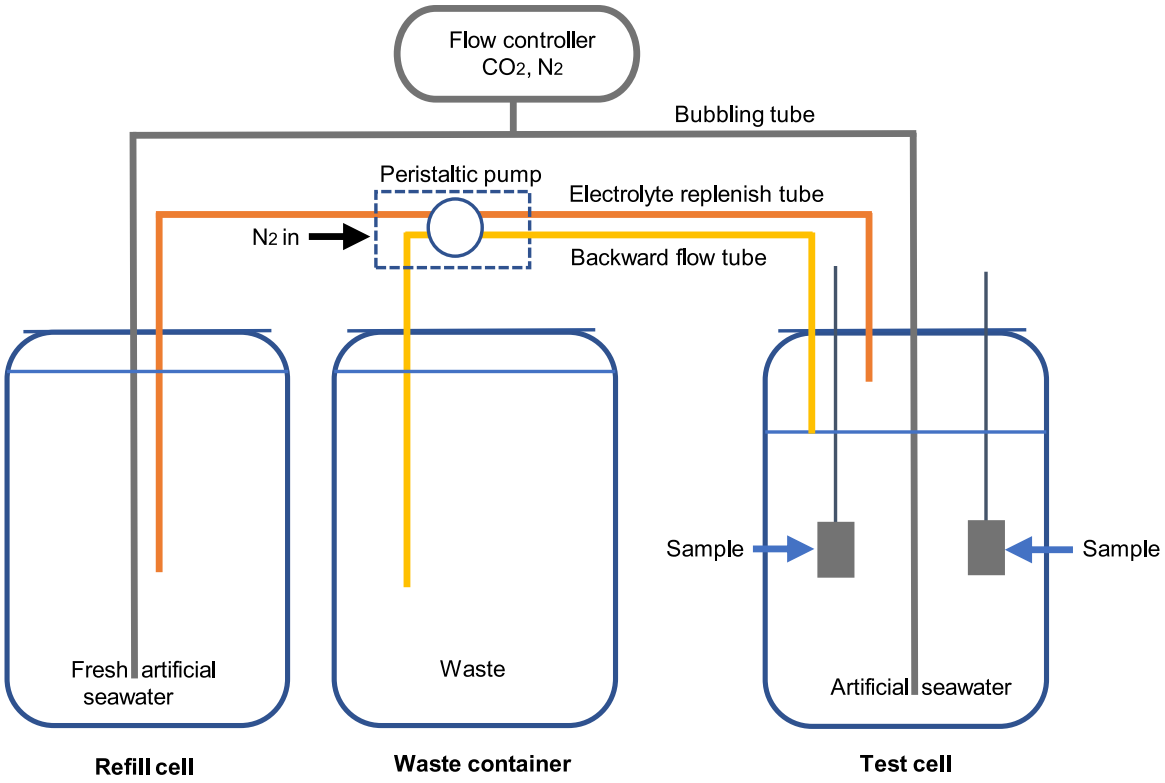

Fig. 1. Schematic of the corrosion test setup used for the CO_2 exposure. The test cell is replenished by fresh artificial seawater in CO_2 environment experiment, while in CO_2/H_2S environment experiment the precipitation of FeS kept the concentration of the dissolved Fe^{2+} ions low and therefore the test cell is not replenished by fresh artificial seawater.

For corrosion testing, the studied materials were cut into rectangular specimens with a length of 12 mm and the same widths and thickness as those of the wires. All surfaces of the specimens were ground with 320 grit SiC paper, washed in acetone and isopropanol in an ultrasound bath, and dried.

Another set of samples was prepared for microstructural analysis by grinding abrasive papers up to 4000 grit SiC, followed by mechanical polishing with 3 μm and 1 μm diamond suspensions, and finally etching in 2% nital solution.

2.2. Corrosion tests

Modified $ASTM$ $D1141$-90 [43] seawater (without calcium chloride to avoid the formation of calcium carbonate ($CaCO_3$) [44]) was used as the corrosion test electrolyte. Its chemical composition is presented in Table 2. A schematic of the corrosion test setup is shown in Fig. 1. The corrosion tests were performed in a setup comprising two parts: the test cell, where the test specimens were immersed in the test electrolyte, and the refill cell, which contained the fresh electrolyte required to replenish the electrolyte in the test cell. The test cell was filled with the test electrolyte and continuously purged with the required gas mixture. The electrolyte was gently stirred and maintained at 25 °C in a water bath. To achieve the required gas composition and feed the test cell, a gas-dosing system based on *Bronkhorst* mass flow controllers was used to blend N_2, CO_2, and H_2S. The refill cell was maintained at room temperature and purged with the same gas composition as that of the test cell.

Table 2
Chemical composition of the corrosion test electrolyte [43].

Compound	NaCl	$MgCl_2$	Na_2SO_4	KCl	$NaHCO_3$	H_3BO_3	$SrCl_2$
Content (g/l)	24.53	5.2	4.09	0.695	0.201	0.027	0.025

The electrolyte was circulated between the test cell and refill cell using a peristaltic pump equipped with $Tygon$ and PVC tubes. The flow rates were controlled by the tubing diameter and the rotation speed of the pump. To avoid oxygen contamination, the pump was placed in a chamber purged with N_2. When the peristaltic pump was on, the flow of liquid into the test cell was continuous and had a maximum rate of 4 ml/min (using a 1.143 mm tubing diameter). The backward flow had a maximum rate of 18 ml/min (using a 3.175 mm tubing diameter) and was self-regulated by draw-off to eliminate the risk of overflowing the test cell. The backward flow was directed to a waste container. The pH value was continuously recorded. The pH increased slightly (between 5.77 and 6.08) during both the CO_2 and CO_2/H_2S exposure experiments. The test cell electrolyte was sampled frequently during exposure to analyze its Fe^{2+} ion concentration. The Fe^{2+} ions were converted to a colored Fe complex, which was photometrically quantified. The electrolyte was continuously replaced by fresh electrolyte (with no dissolved corrosion products) at a flow rate of ca. 0.8–1.6 l/day to ensure a low concentration of Fe^{2+} (less than 80 ppm in the test cell).

Two sets of experiments were performed in the above-mentioned setup: first, the test cell was purged with 0.2 bar CO_2, and second,

with 0.2 bar CO_2 and 1 mbar H_2S, with a total flow rate of 200 ml/min. In the second test set, because the precipitation of FeS kept the concentration of the dissolved Fe^{2+} ions low, no electrolyte replacement was required. Each set of experiments was performed in three rounds, and the duration of both sets of tests was 504 h (21 d). Thus, the experimental setup used for the CO_2/H_2S exposure consisted of only the test cell and the corresponding gas flow line, see Fig. 1.

2.3. Corrosion rate measurements

The corrosion rates of all the studied materials in both experimental sets were measured using the linear polarization resistance (LPR) and were determined by weight-loss method. LPR measurements were performed using a regular 3-electrode electrochemical setup, with a titanium spiral as the counter electrode and a carbon steel cylindrical specimen as the pseudo-reference electrode. A $Gamry\ PC3/750$ potentiostat with $ECM8$ multiplexer and $CMS105$ software were used for the LPR measurements. The procedure used to interpret LPR data is generally based on the methodology described in the literature [45–47]. A linear potential sweep was applied to the working electrode from −5 mV to 5 mV vs. the OCP. Within this restricted potential range, the resulting current response can be considered linear, allowing the polarization resistance (R_p) to be calculated as the slope of the potential (E) vs. current (I) plot:

$$R_p = \frac{\delta E}{\delta I} \tag{11}$$

The corrosion current density (i_{corr}) was subsequently calculated using the Stern–Geary equation [45,48], where B is the Stern–Geary coefficient and A is the specimen area.

$$i_{corr} = 10^6 \frac{B}{R_p A} \tag{12}$$

The Stern–Geary coefficient (B) is related to the Tafel slopes of the anodic and cathodic half-reactions, that is, β_a and β_c:

$$B = \frac{\beta_a \beta_c}{2.3(\beta_a + \beta_c)} \tag{13}$$

In the absence of Tafel slopes, the B coefficient was determined from the weight loss data. The corrosion current density, steel density, and Fe molar mass were then used to calculate the corrosion rate (CR) or penetration rate using Faraday's law. All relevant constants were included, which simplifies to:

$$CR\ (\mathrm{mm/y}) = 1.16 i_{corr}\ (\frac{\mathrm{A}}{\mathrm{m^2}}) \tag{14}$$

To perform the weight-loss method, the samples were weighed using an analytical balance with an accuracy of $\pm 10^{-4}\ g$ before and after the corrosion test. After the corrosion products were removed by immersing the samples in $Clarke's$ solution (inhibited hydrochloric acid, that is 36% HCl containing 50 g/l $SnCl_2$ and 30 g/l $SbCl_3$) for 1 min according to $ASTM$ standard G 1-03 [49]. The weight loss of the samples was used to calculate the average corrosion rate of each carbon steel sample using the following equation:

$$CR\ (\mathrm{mm/y}) = 8.76 \times 10^4\ \frac{\mathrm{W}}{\rho \mathrm{A} t} \tag{15}$$

where W is the weight loss of the sample in grams, A is the total area of the sample in cm^2, t is the immersion time in hours, ρ is the density of the material in g/cm^3, and 8.76×10^4 is the unit conversion constant [50,51]. It should be noted that using this method, a corrosion rate that is averaged over the entire exposed area is obtained for a specific sample.

2.4. Cross-sectional characterization of corrosion layers

To observe the morphology and thickness of the corrosion layers formed on the specimens exposed to the CO_2 environment, the samples were embedded in $DuroCit-3kit$, an acrylic resin that is suitable for the protection of the corrosion layers. After the curing time, the embedded samples were cut. Then, the cross-sectioned samples were ground up to 4000 grit with SiC abrasive paper and polished with 3 μm and 1 μm diamond suspensions.

The corrosion layers formed on the specimens exposed to the CO_2/H_2S environment were on the nanometer scale, and the embedding process could damage the layer. Therefore, a focused ion beam (FIB) was employed to characterize the cross-sections of the specimens exposed to the CO_2/H_2S environment. Prior to the cross-sectional observation by ion beam-induced secondary electron imaging, two platinum protection layers with thicknesses of 1 μm using an electron beam and 1.5 μm using an ion beam were applied on a selected area on the sample surfaces to protect the corrosion layer from potential damage by the ion beam.

2.5. X-ray photoelectron spectroscopy analysis

The chemical composition of the corrosion layers was determined using X-ray photoelectron spectroscopy (XPS) performed on a $VG\ Escalab\ 220i\text{-}XL$ spectrometer. The samples were transferred for XPS analysis inside a desiccator to minimize exposure to the open environment. XPS analysis was performed using a $Kratos\ Axis\ Ultra\ DLD$. A monochromatic Al $K\alpha$ source (12 mA, 12 KV) was used for spectrometry. The sample analysis chamber pressure was 1×10^{-9} Torr (0.13 μPa) during the operation. Elemental maps were collected with a pass energy of 120 V using two sweeps. High-resolution regional acquisitions were performed with a pass energy of 20 V using ten sweeps and 0.1 eV step size for each element. The analysis area was 300 × 700 μm^2, and five areas were analyzed for each sample. Argon sputtering with an energy of 4 KV was used for 30 s to remove surface contamination before the start of the XPS analysis. Regional peaks were fitted by Shirley background subtraction Using $Casa\ XPS$ software. For curve fitting, evaluation, and quantification, $Gaussian/Lorentzian$ asymmetry was used, and the full width at half maximum ($FWHM$) was kept constant for the oxide components.

3. Results

3.1. Materials characterization

Fig. 2 shows SEM micrographs from the surface view of the studied materials at two magnifications. Material $CS28$ is a low-carbon steel (Table 1) with both large and small drawn ferritic grains, including different types of small ferrite sub grains. The cementite particles continuously precipitated mainly along the grain boundaries, while a small fraction of cementite particles was dispersed inside the ferrite grains. The ferrite grains were oriented along the drawing direction.

Materials $CS62$ and $CS65$ are high-carbon steels that exhibited a ferrite–cementite microstructure with small fractions of ferrite. The morphology of the cementite in material $CS62$ consisted of spherical particles or broken lamellae in a ferrite matrix, whereas material $CS65$ showed a pearlite microstructure with thick lamellae of cementite in a ferrite matrix (Fig. 2). The ferrite grain size and connection network between the ferritic grains were larger in material $CS65$ than in material $CS62$. Material $CS83$ was a hypereutectoid high-carbon steel that exhibited a predominantly lamellar pearlite microstructure with a lower fraction of ferrite than the other materials.

The ferrite, cementite, and pearlite phase fractions for all materials were determined by image analysis using ImageJ $Fiji$, and the data are listed in Table 3. The pearlite colonies had different interlamellar spacings in the materials $CS65$ and $CS83$. The average interlamellar spacing measured by $Fiji$ shows that material $CS83$ had finer pearlite with an average interlamellar spacing of 117±30 nm than material $CS65$ with an average interlamellar spacing size of 242 ± 64 nm (Table 3).

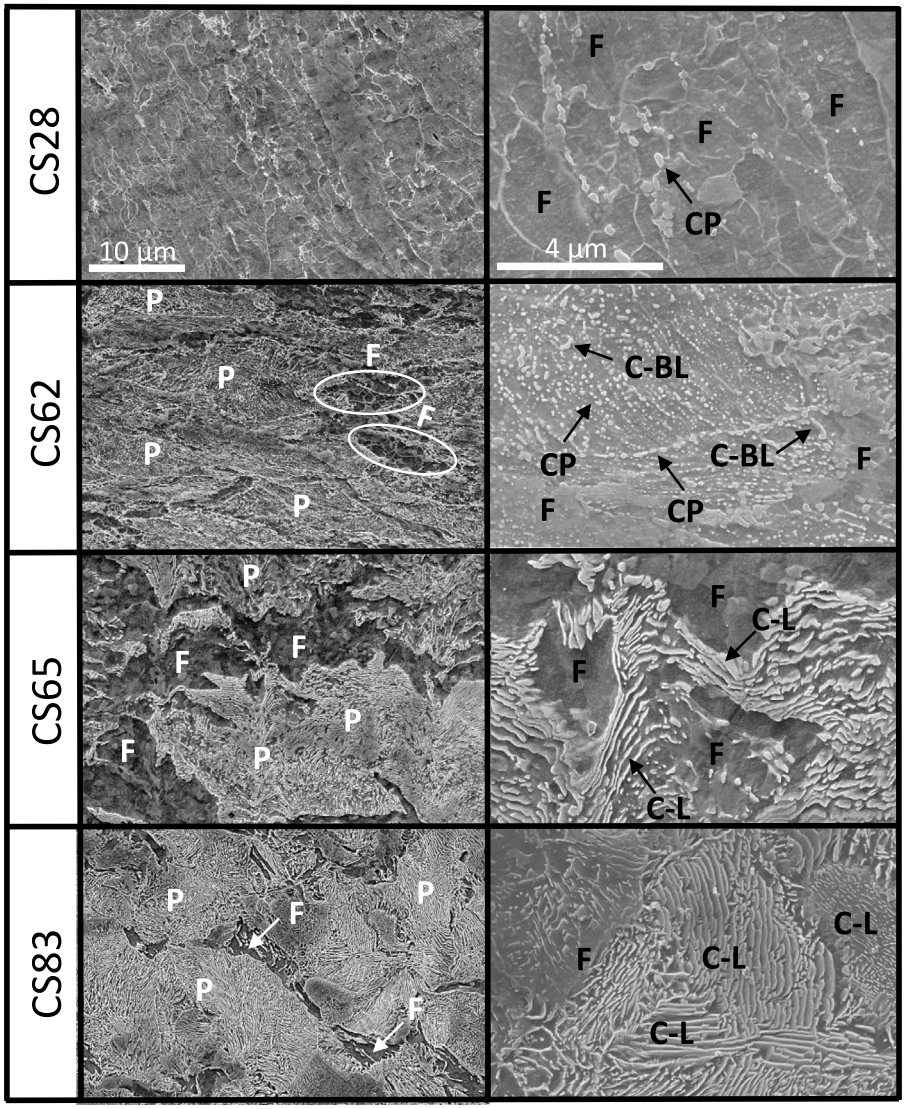

Fig. 2. *SEM* micrographs of the studied materials surface. The right column shows the high magnification images of the microstructure of the materials. The magnification of the *SEM* images in each column is the same for all materials. The ferrite and pearlite phases are marked by F and P, respectively. The cementite particles, cementite lamellae, and broken lamella of cementite are marked by C-P, C-L, and C-BL, respectively.

Table 3
Microstructures phase fraction and interlamellar spacing.

Material	Ferrite (%)	Cementite (%)	Pearlite (%)	Interlamellar spacing (nm)
*CS*28	96	4	35	-
*CS*62	91	9	81	-
*CS*65	90	10	85	242-±64
*CS*83	88	12	98	117-±30

3.2. Corrosion rate measurements

The results of the *LPR* measurements for all materials in both CO_2 and CO_2/H_2S environments are summarized in Fig. 3. The curves obtained from the *LPR* measurements were fitted using a polynomial equation. Fig. 3a shows that the corrosion rate in the presence of CO_2 continuously increases with time for all materials, and the curves did not stabilize during the experiments. The corrosion rate increment is high for the materials *CS*65 and *CS*83, both of which have a pearlitic microstructure.

No clear corrosion rate-carbon content/cementite phase fraction relationship is observed in the CO_2/H_2S environment. It can be seen that material *CS*28, which has the lowest corrosion rate in CO_2 environment, showed the highest corrosion rate in the CO_2/H_2S environment, whereas material *CS*83 exhibits the lowest corrosion rate among the studied materials.

Fig. 4 shows the average corrosion rates obtained from the weight loss data for all the studied materials exposed to the CO_2 and CO_2/H_2S environments for 21 d. Error bars represent the standard deviation of the mean value of the weight loss data of the three samples for each material. The weight loss corrosion rate results show that the average corrosion rate of the studied materials increases with the carbon content or cementite phase increment in the CO_2 environment. However, this trend is not observed in CO_2/H_2S environment. As shown in Fig. 4, material *CS*28 had the lowest corrosion rate in the CO_2 environment, and has the highest corrosion rate in the CO_2/H_2S environment. Materials CS62 and CS83 displayed almost the same corrosion rate, while the corrosion rate of material CS65 was higher than both. Therefore, the corrosion rates of the studied materials in the CO_2/H_2S environment does not exhibit a specified trend.

As is shown in Fig. 3b, and Fig. 4b, the presence of H_2S induced a significant reduction in the corrosion rate by one order of magnitude compared to the CO_2 environment. In Fig. 3b, all materials display a high corrosion rate during the first hours of the experiment, when

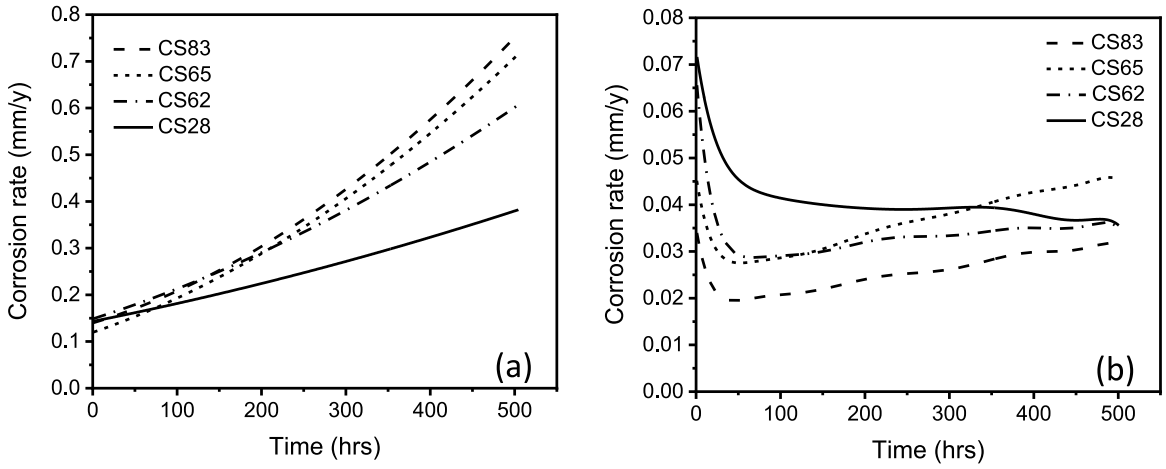

Fig. 3. *LPR* corrosion rates versus exposure time in the 0.2 bar CO_2 environment (a) and the 0.2 bar CO_2/1 mbar H_2S environment (b).

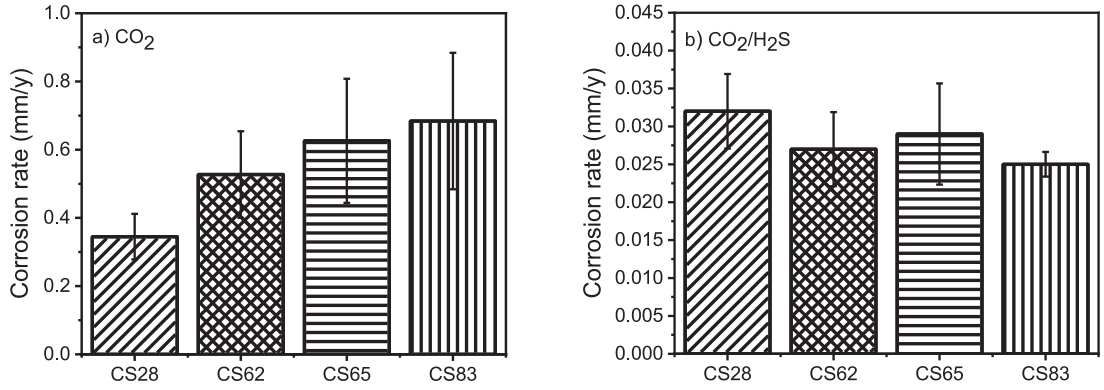

Fig. 4. Corrosion rates calculated from weight loss data after exposure to the 0.2 bar CO_2 environment (a) and the 0.2 bar CO_2/1 mbar H_2S environment (b) for 21 d. The columns show the mean value of three tests and the bars represent the standard deviation of the mean value.

the corrosion layer is not yet protective, and ions can transfer freely through it. Then, the corrosion rate decreases with time until approximately 40 h. Hereafter, the corrosion rate of material $CS28$ is almost stabilized, while the corrosion rates of materials $CS62$, $CS65$, and $CS83$, show a slight increase, with the highest corrosion rate increase in material $CS65$. It should be noted that these data are based on the results obtained in the performed experiments' time frame (21 d). The corrosion rates of all the studied materials can be changed over a longer period of time.

3.3. Corrosion layer characterization

To provide satisfactory protection, the corrosion layer should exhibit good adhesion and full coverage of the sample surface. In addition, the corrosion layer thickness, porosity, and composition, are important criteria for creating a protective layer that can significantly affect the corrosion rate [52–54]. The results that demonstrate and evaluate these criteria are presented in the following sections.

3.3.1. Corrosion layer morphology and thickness

Fig. 5 shows the surface morphology of the corrosion layers formed on all materials after 21 d of exposure in the CO_2 and CO_2/H_2S environments. In the CO_2 environment, by comparing the SEM images, the surface of the corrosion layer formed on material $CS28$ seems to have an uneven and rough appearance. This roughness is low for materials $CS62$ and $CS65$, whereas for material $CS83$ the corrosion layer exhibits a more compact and uniform appearance. The differences between the corrosion layer interface appearances are more evident in the cross-sectional SEM images shown in Fig. 6. Both the corroded sample surface/corrosion layer interface (shown by the green line (1) in Fig. 6 $CS28$) and the surface of the corrosion layer (shown by the red line (2) in Fig. 6 $CS28$) are quite uneven for material $CS28$, whereas they are almost uniform for materials $CS62$ and $CS83$. Material $CS65$ exhibits some localized corrosion at the corroded sample surface/corrosion layer interface.

A substantial reduction in the corrosion layer thickness was observed in the materials exposed to the environment containing 1 mbar H_2S compared with the samples in the pure CO_2 environment. By comparing the corrosion layer thicknesses of different materials, an increase in thickness was observed with increasing carbon content in both the CO_2 and CO_2/H_2S environments, as shown in Fig. 6. Materials $CS62$ and $CS65$ show almost similar corrosion layer thicknesses in the CO_2 environment, and the corrosion layer thickness of material $CS65$ is slightly lower than that of material $CS62$. In the CO_2/H_2S environment, the same trend is observed, which means that the corrosion layer thickness increases with increasing carbon content; however, the corrosion layer thickness of material $CS65$ is significantly lower than that of the other two high-carbon materials, $CS62$ and $CS83$, and it is closer to that of material $CS28$.

3.3.2. Corrosion layer chemical composition

The chemical compositions of the surface and cross-section of the corrosion layer were analyzed using XPS and EDS, respectively. Fig. 7 represents the entire range of binding energies from 0 to 1200 eV of the material $CS65$ corrosion layer (the full spectrum of all materials is similar). The peaks for Fe $2p$, O $1s$, and C $1s$, are visible in all the carbon steel surfaces in both the CO_2 and CO_2/H_2S environments, whereas the S $2p$ peak is only observed in the CO_2/H_2S environment.

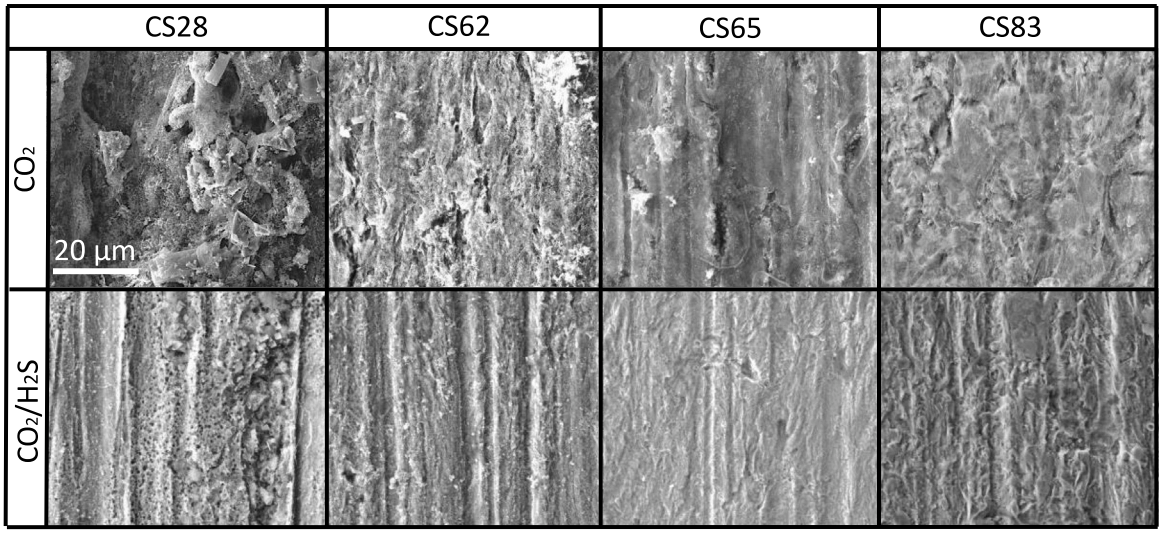

Fig. 5. *SEM* micrographs of the surface morphology of carbon steel samples after exposure to the 0.2 bar CO_2 environment (first row) and the 0.2 bar CO_2/1 mbar H_2S environment (second row) for 21 d.

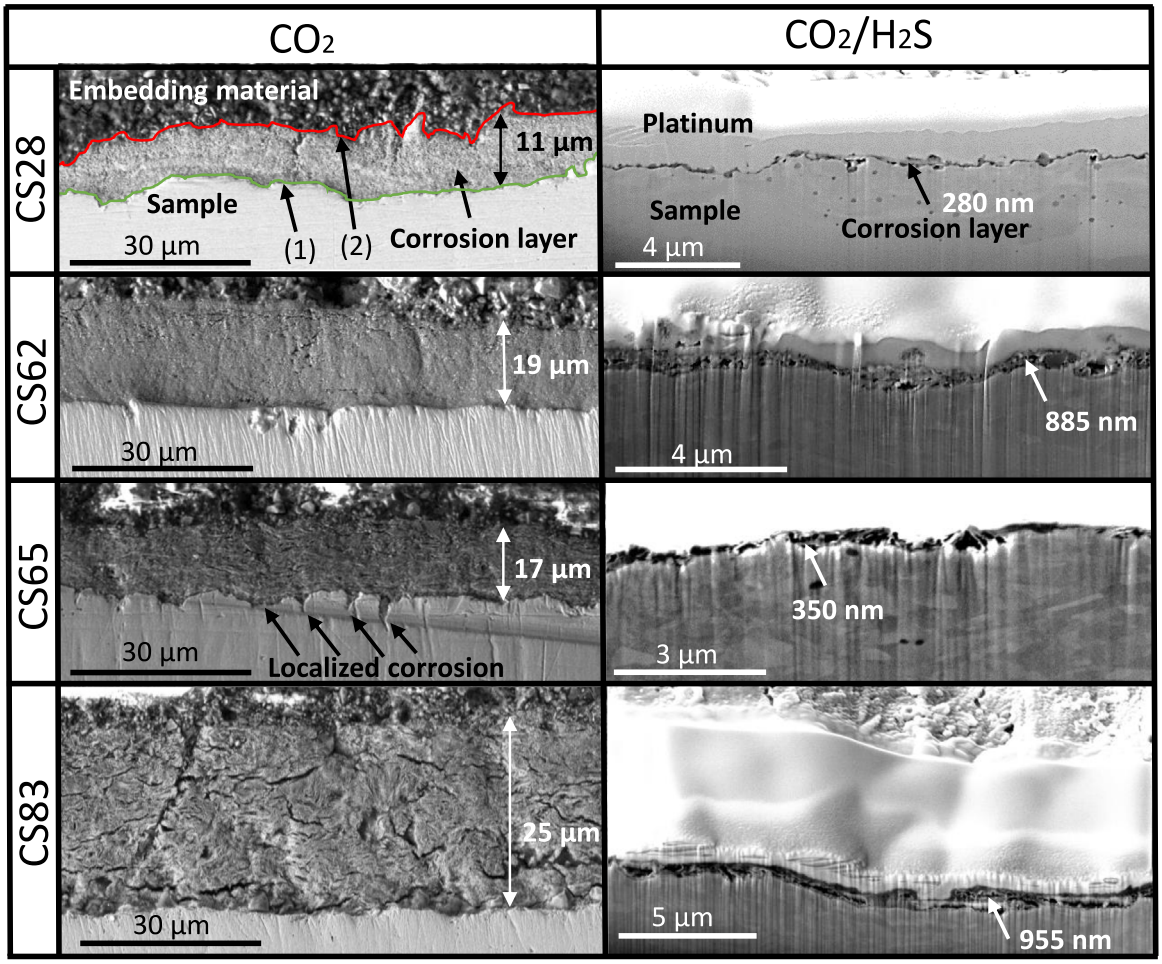

Fig. 6. Cross-section morphologies of the corrosion layers of the studied materials exposed to 0.2 bar CO_2 (left column) and the 0.2 bar CO_2/1 mbar H_2S (right column) environments for 21 d. The surface of the samples, exposed to the 0.2 bar CO_2/1 mbar H_2S environment, were covered with platinum before milling to protect the nano-scale corrosion layers. The numbers written in each image denote the average thickness of the corrosion layers of two samples for each material and environment. For CO_2 exposure, the thicknesses are shown by double arrows. For CO_2/H_2S exposure, the thicknesses are pointed by arrows because they are thin.

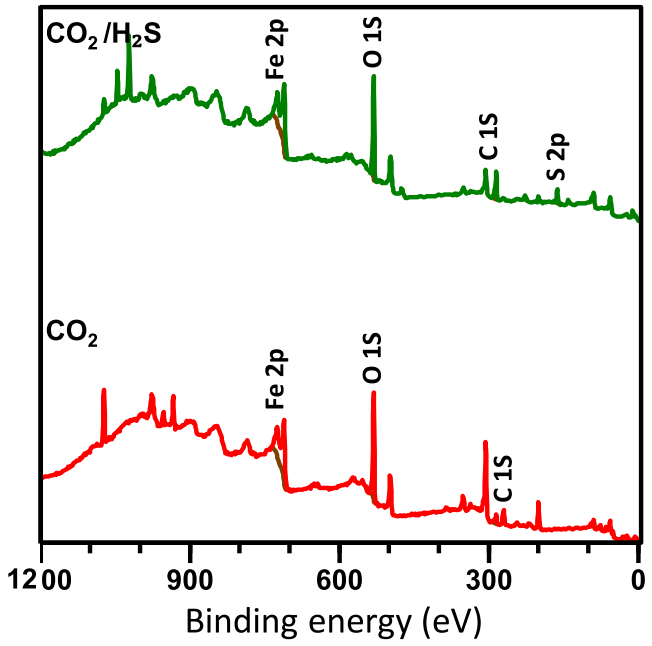

Fig. 7. *XPS* overview spectrum obtained from the surface of the material *CS*65 after 21 d exposure to the 0.2 bar CO_2 and 0.2 bar CO_2/1 mbar H_2S environments.

Table 4
Relative intensities (in atomic percent) of the C 1*s* signals for the corrosion layers formed in the 0.2 bar CO_2 environment.

Material	$FeCO_3$	C–Cl	C–C
*CS*28	4.56	15.54	79.89
*CS*62	10.56	18.67	70.76
*CS*65	11.64	9.05	79.29
*CS*83	9.01	19.44	71.54

Table 5
Relative intensities (in atomic percent) of the *O*1*s* signals for the corrosion layers formed in the 0.2 bar CO_2 environment.

Material	$FeCO_3$	Fe_2O_3
*CS*28	86.27	13.72
*CS*62	70.59	29.4
*CS*65	56.94	43.05
*CS*83	55.58	44.41

The regional spectrum of the carbon 1*s* is shown in Fig. 8 for all materials exposed to the CO_2 environment. All spectra were deconvoluted into three evident peaks around 284.5–285.5 eV, 286–287 eV, and 288–290 eV. The first peak at 284.5–285.5 eV corresponds to adventitious carbon, which is always introduced to the samples from the environment. The second peak at 286–287 eV can be attributed to a compound of carbon with chlorine or carbon with oxygen [55]. The third small peak at 288–290 eV displays the presence of $FeCO_3$ [56]. The relative intensities of the C 1*s* signals for each peak are listed in Table 4 for all materials. The $FeCO_3$ peak exhibits a high intensity in the materials *CS*65, *CS*62, and *CS*83, and material *CS*28 shows the lowest $FeCO_3$ intensity.

The second column of Fig. 8 presents the deconvoluted peaks of the *XPS* spectrum of oxygen 1*s* for each material. The first peak at 530–530.5 eV is specified as ferric oxide (Fe_2O_3), and the second peak at 531.7–532 eV is attributed to $FeCO_3$ [55]. The relative intensities corresponding to each peak are presented in Table 5.

The *XPS* spectrum for the Fe 2*p* region of each material is presented in the third column of Fig. 8 and the relative intensities of the deconvoluted peaks are listed in Table 6. The Fe^{2+} peak which is

Table 6
Relative intensities (in atomic percent) of the Fe2*p* signals for the corrosion layers formed in the 0.2 bar CO_2 environment.

Material	Fe^{2+}	Fe^{3+}	Fe
*CS*28	57.39	39.16	3.44
*CS*62	44.05	50.78	5.15
*CS*65	36.42	60.46	3.1
*CS*83	26.09	70.19	3.7

Table 7
Relative intensities (in atomic percent) of the Fe2*p* signals for the corrosion layers formed in the 0.2 bar CO_2 1 mbar H_2S environment.

Material	Fe^{2+}	FeS	Fe^{3+}	FeS_2
*CS*28	6.91	52.12	25.05	5.91
*CS*62	21.45	46.43	15.49	16.61
*CS*65	10.87	56.51	3.4	29.2
*CS*83	6.64	66.47	11.11	15.76

present at 712–714 eV is obvious in all materials. This peak can be attributed to the presence of $FeCO_3$ on the top surface of the corrosion layer [57,58]. However, this can also be related to $Fe(OH)_2$ [59]. Two other peaks around 709.5–710.5 eV and 706.5–707.5 eV are related to Fe^{3+} iron compounds, such as ferric oxide (Fe_2O_3) and pure iron, respectively [58]. According to the peak intensities of different materials shown in Table 5 for O 1*s* and Table 6 for Fe 2*p*, the intensity of Fe^{2+} decreases and the intensity of Fe^{3+} iron compounds increases with increasing carbon content. Material *CS*83 exhibits the highest amount of Fe^{3+} iron compounds and the lowest amount of Fe^{2+} compounds. The presence of iron metal at 706.5 to 707.5 eV, observed for all materials, can be the result of Ar^+ sputtering, and it cannot be related to the uncorroded ferrite [35]. Ion bombardment can cause physical and chemical changes, and reduce Fe_3O_4, Fe_2O_3, and FeO, on the surface. This reduction can be attributed to the shift in intensity from the Fe^{3+} position at 711.2 eV to low binding energies in the present study *XPS* results (709.5- 710.5 eV), and even to a mixture of Fe^{3+}, Fe^{2+}, and iron metal [60,61].

Fig. 9 presents the *XPS* spectra of S 2*p* and Fe 2*p* for the corrosion layer formed on each material after exposure to the CO_2/H_2S environment. The two peaks at 710.5–711.5 eV and 708–709 eV correspond to mackinawite (FeS) and pyrite (FeS_2), respectively, in the Fe 2*p* scan for all materials in Fig. 9 [7,62]. FeS and FeS_2 peaks in the S 2*p* spectrum at approximately 163.3 and 161.6 eV confirm the presence of these two compounds in the corrosion layers formed in the CO_2/H_2S environment. Moreover, *XPS* analysis revealed the presence of Fe^{2+} and Fe^{3+} iron compounds in the CO_2/H_2S environment.

The relative intensities of the deconvoluted FeS and FeS_2 peaks for Fe 2*p* are listed in Table 7. The sum of FeS and FeS_2 intensities for each material reveals that the mackinawite and pyrite intensity increase with increased carbon content, and materials with pearlitic microstructures (*CS*65 and *CS*83) exhibit almost similar FeS and FeS_2 intensities (85 and 81, respectively). The corrosion layers of materials *CS*62 and *CS*28 are richer in Fe^{2+} and Fe^{3+}-related compounds compared to materials *CS*65 and *CS*83.

It should be noted that the *XPS* data were collected from the surface of the corrosion layer at a depth of approximately 5 nm. Therefore, *EDS* was performed on the cross-sections of the *CS*28 and *CS*83 corrosion layers to verify the presence of the main elements that are recognized by *XPS*. Because the corrosion layers formed on the materials exposed to the CO_2/H_2S environment are quite thin (less than 1 μm), the conditions for performing the *EDS* analysis on their corrosion layer cross-sections are not ideal, and the *EDS* analysis is only performed on the materials that are exposed to the CO_2 environment. The presence of the main elements of the corrosion layers, Iron, Oxygen and Carbon, was verified in *EDS* results in Fig. 10. The scan shows the *EDS* elemental concentration profile along the yellow line

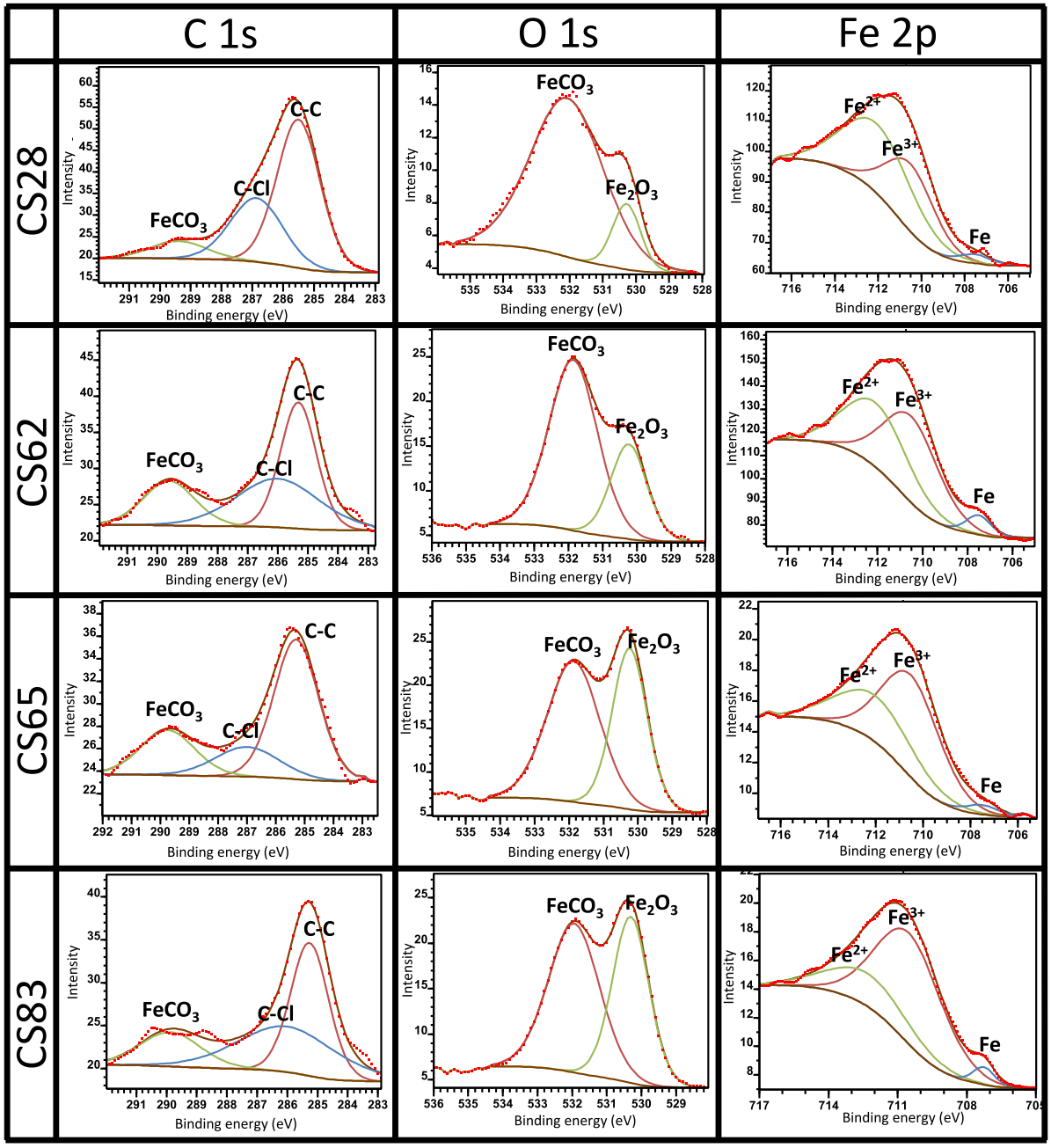

Fig. 8. Regional *XPS* spectrum of C, O, and Fe for the corrosion layer formed on the surface of all materials exposed to the 0.2 bar CO_2 environment.

for each material. The iron intensity (green line in the graphs) is at a high density where the scan line passes the material; then, it decreases to a high extent where the corrosion layer appears. In material *CS*28 the iron intensity was higher in the corrosion layer area than in material *CS*83. In addition, material *CS*28 presents a high oxygen intensity in the corrosion layer, while carbon has the highest intensity in the corrosion products of material *CS*83. As the embedding material begins to appear, the carbon and oxygen intensities are quite high (because an acrylic mounting system is used to embed the samples), and the iron intensity decreases to zero.

3.3.3. Corrosion layer porosity

Porosity is a crucial factor in determining the protective role of the corrosion layer by facilitating ion migration. *FIB* was used to investigate the porosity to obtain a more obvious view of the corrosion layer cross-section. The *SEM* images of the cross-sections prepared using *FIB* are shown in Fig. 11. By comparing material *CS*28 with materials *CS*65 and *CS*83, it is obvious that the corrosion layer formed on the lamellar and high-carbon microstructure (Fig. 11b and c) is quite porous, and the cross-sectional appearance of the corrosion layer formed on material *CS*28 (Fig. 11a) is more closely-packed. Interestingly, the corrosion layer formed on the pearlitic materials consisted of two zones: the combination of iron carbide (Fe_3C) and corrosion product on top (Fig. 11b and c). The corrosion product can be a combination of $FeCO_3$, $Fe(OH)_2$, Fe_2O_3, and other Fe^{2+} and Fe^{3+} compounds. In material *CS*65 (Fig. 11b), the porosity of the corrosion layer was high in the vicinity of the sample surface, and decreases through the thickness of the corrosion layer towards the surface of the corrosion layer. However, for material *CS*83 (Fig. 11c), the porosity is almost evenly distributed throughout the thickness until the second layer,

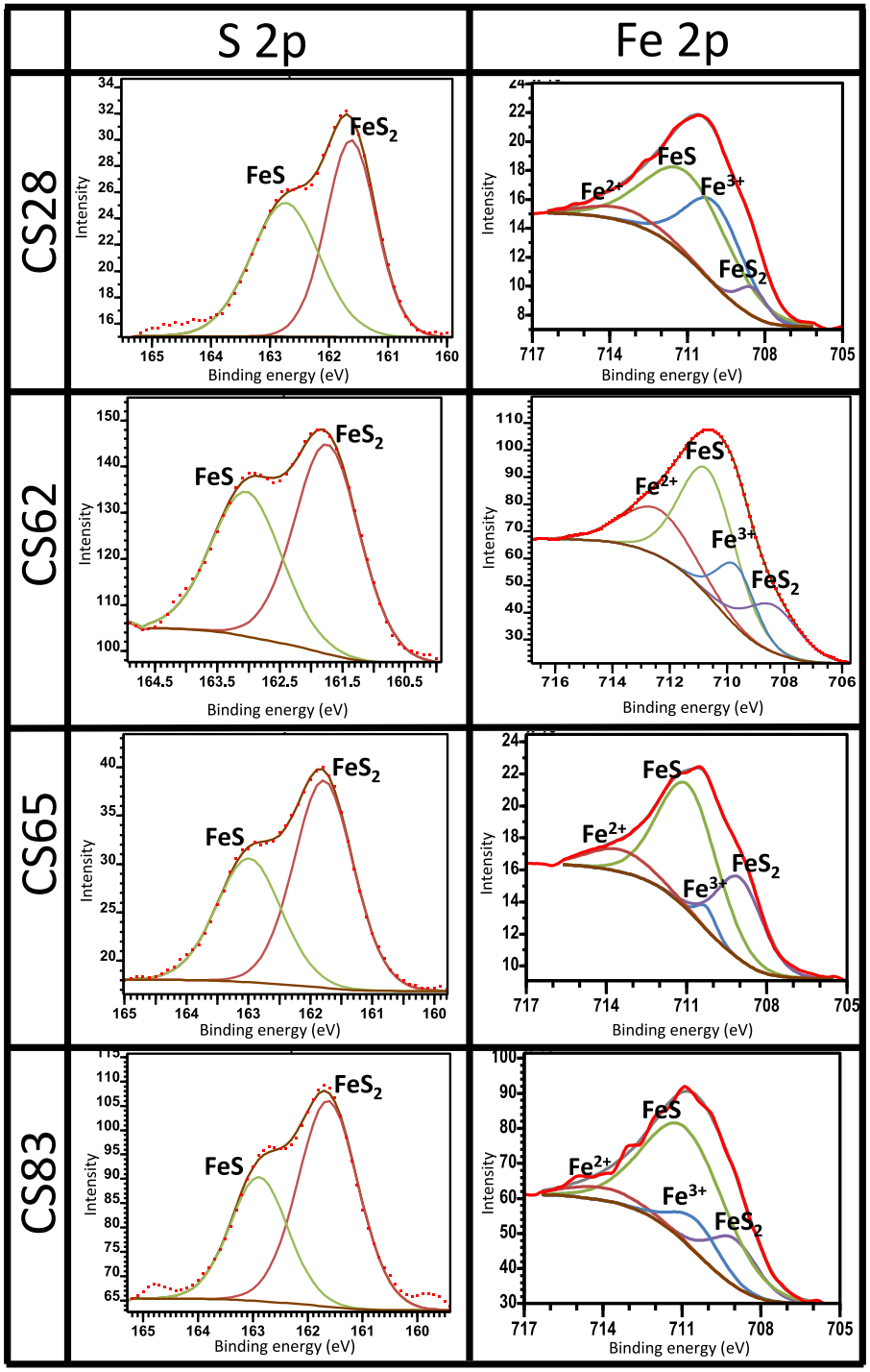

Fig. 9. Regional XPS spectrum of S and Fe from the corrosion layer formed on all materials in the 0.2 bar CO_2/1 mbar H_2S environment.

and its thicker corrosion layer corresponds to a high concentration of porosity and inhomogeneity in the corrosion layer compared with the appearance of the corrosion layer on material *CS*65.

4. Discussion

4.1. CO_2 environment

4.1.1. Corrosion rates

Fig. 3a, and Fig. 4a show the corrosion rate obtained from the LPR measurements and the weight loss data in the CO_2 environment, respectively. A comparison between the different materials showed that the corrosion rate increased with increasing carbon content and cementite phase fraction. As discussed in previous studies [63–66], the presence of cementite and ferrite in carbon steels can accelerate the corrosion rate because cementite is more corrosion-resistant than iron [65]. Therefore, cementite functions as a cathodic site, and a galvanic couple is formed between the cementite region and ferrite matrix, which leads to a high ferrite corrosion rate. The effect of cementite as the cathodic area is reported to be significant in carbon steels with carbon content higher than 0.15 wt% [67]. In this study, all steels had a carbon content higher than 0.15 wt%.

In carbon steels with pearlitic microstructures, such as materials *CS*65 and *CS*83, the cementite phase is arranged in layers. When the

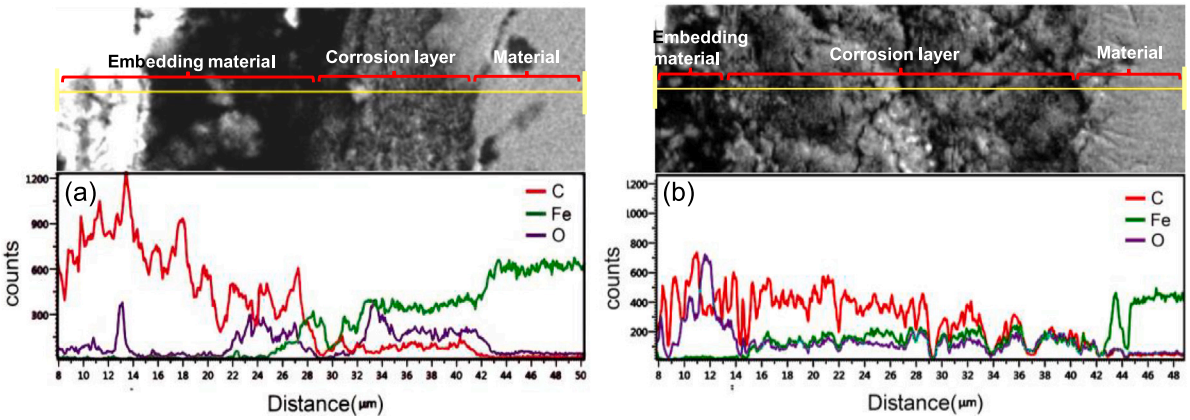

Fig. 10. EDS line Scan through the corrosion layers formed on materials $CS28$ (a) and $CS83$ (b) after exposure to the 0.2 bar CO_2 environment.

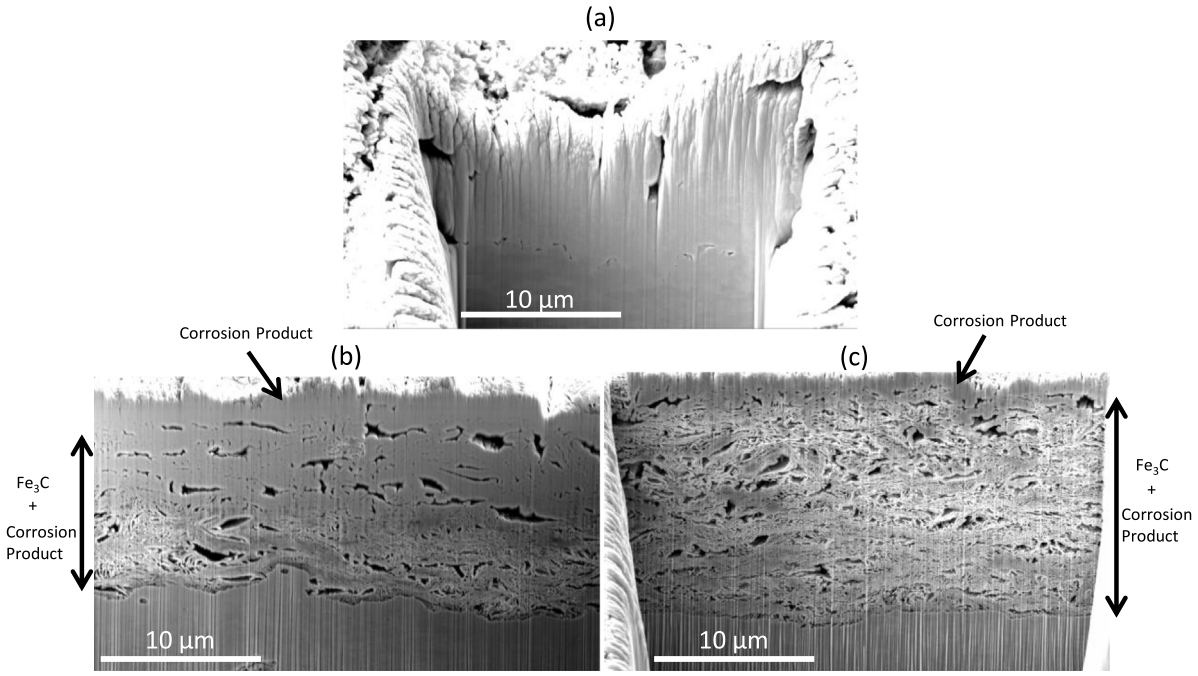

Fig. 11. $FIB-SEM$ micrographs of the corrosion layers formed in the 0.2 bar CO_2 environment on materials $CS28$ (a), $CS65$ (b), and $CS83$ (c). The scale bars show the surface dimensions not the cross-sections.

ferrite phase between the cementite layers is dissolved, the corrosion products can be trapped between the remaining cementite layers to form a physical hindrance between the ferrite and electrolyte, which in turn can decrease the corrosion rate [68]. However, the role of cementite in anchoring the corrosion layer and creating a barrier between the steel surface and the electrolyte can be ineffective in this study because of the low concentration of Fe^{2+}, which causes non-uniform coverage of the corrosion layer. The LPR measurements (Fig. 3a) show that the corrosion rates continuously increased with time, and the curves did not stabilize during the experiments. Furthermore, LPR measurements in the CO_2 environment displayed an increment in the gradient of the curves with increased carbon content, and the lamellar microstructures ($CS65$ and $CS83$) showed the highest slopes. This is attributed to the large area of cementite owing to the increase in carbon content and the galvanic effect of cementite, which is in good agreement with the study performed by Gulbrandsen et al. on $X65$ and $St52$ carbon steels exposed to the CO_2 environment [69].

In addition to the role of cementite in accelerating the corrosion of the ferrite phase, the volume fraction, distribution, and morphology of cementite, can play a crucial role in the corrosion layer formation and consequently affect the corrosion rate [33,52–54]. For instance, the carbon content of material $CS65$ is close to that the carbon content of material $CS62$ (Table 1), while its microstructure is similar to that of material $CS83$'s (since both have the pearlitic microstructure Fig. 2) and its corrosion rate is also more close to the corrosion rate of material $CS83$ than material $CS62$ (Fig. 3a). It can be deduced from this comparison that the microstructure and cementite morphology can have a more critical role in the corrosion rate than the carbon content or cementite fraction. To study the cementite morphology effect on the formation of corrosion products, the XPS, EDS, SEM and FIB results were analyzed.

4.1.2. Chemical characterization of corrosion layers

The XPS results from the top surface of the corrosion layer, as shown in Fig. 8 show that the corrosion products formed in all the studied materials in CO_2 environment contain Fe^{2+} iron compounds. Based on the C $1s$, O $1S$ spectrum analysis, the Fe^{2+} peak is related to the presence of $FeCO_3$. In the analysis of Fe $2p$ spectrum, this peak is at 712–714 eV for all the studied materials, which is as approximately identical to the $FeCO_3$ peak range shown in the XPS Hand book.

However, because the binding energies of different iron compounds in the Fe 2*p* spectrum are very close, it is noted in the previous sections that this peak can also be related to other Fe^{2+} compounds, such as iron hydroxide ($Fe(OH)_2$). $FeCO_3$ is a common corrosion product formed on steels in CO_2 environments. The key factor for the formation of $FeCO_3$ is the supersaturation of Fe^{2+} and CO_3^{2-} ions (Eq. (8)) [70]. In this study, to simulate worst-case corrosion (i.e., when the formation of protective corrosion layers is hindered), the Fe^{2+} concentration was kept low (less than 80 ppm which is a critical point for $FeCO_3$ formation based on the experimental conditions in this study [71]) during the exposure, and this condition is not favorable for $FeCO_3$ scale formation. It is important to emphasize that the *XPS* is a surface analysis technique that exhibits data from the top surface (5–10 nm) of the corrosion layer. Therefore, the presence of $FeCO_3$ in the corrosion layer bulk and between the remaining Fe_3C layers or particles cannot be proven by *XPS* in this study. Nešic et al. [70] discussed in their study that in CO_2 corrosion, the chemical conditions on the surface of the steel can be completely different than the conditions in the bulk solution. Because of the corrosion process, Fe^{2+} ions are produced, whereas H^+ ions are consumed on the surface of the corroding steel. This process results in a higher *pH* at the surface of the metal than in the bulk solution. The inverse dependence of H_2CO_3 reduction on *pH* [72] causes an increase in CO_3^{2-} concentration at the surface because of the high local *pH*. This means that at the surface of the metal, a lower Fe^{2+} concentration is required to reach the saturation limit of $FeCO_3$ [73]. Therefore, $FeCO_3$ can also exist in the bulk of the corrosion layer owing to the different chemical conditions at the surface of the metals.

However, as discussed by Rémazeilles et al. when the Fe^{2+} or carbonate dissolved species concentrations are insufficient, $Fe(OH)_2$ is the most probable compound that can be precipitated as corrosion products [74]. It can be assumed that although the *XPS* analysis of the top layer of the corrosion products demonstrates the presence of $FeCO_3$, because the bulk solution chemistry is not favorable for $FeCO_3$ formation, the corrosion layer can be $FeCO_3$ and/or $Fe(OH)_2$. These are formed between the remaining Fe_3C layers or particles in the bulk of the corrosion layers.

Because all the studied materials contained cementite (Fe_3C) in their microstructures (Table 3), and considering that Fe_3C was not dissolved during the corrosion process because of the galvanic effect between ferrite and cementite, it was expected that the corrosion layer contained the remaining Fe_3C. However, the *XPS* results did not display the Fe_3C peak for any of the studied materials. According to Fig. 11b and c, the first few micrometers of the corrosion layer surface consisted of $FeCO_3$ and/or other Fe^{2+} and Fe^{3+} compounds, and no peaks corresponding to Fe_3C were observed in the *XPS* analysis. Since the *XPS* data were collected from the corrosion layer surface, the inner corrosion layer composition was not detected by this technique. Therefore, the inner corrosion layer that is marked by Fe_3C + corrosion product in Fig. 11b and c is based on the *EDS* line scan (Fig. 10) and the similar results in the previous studies [52,59]. Lopez et al. [35] showed in their study that only after 10 min of Ar^+ sputtering, a new peak indicating the presence of Fe_3C appeared at approximately 283 eV. The *EDS* line scan from the cross-sections of the corrosion layers formed on materials *CS*28 and *CS*83 in Fig. 10 confirms the presence of carbon, iron, and oxygen in the corrosion products. The high carbon intensity in the corrosion products of material *CS*83 can be explained by the presence of a high amount of Fe_3C in its corrosion product. In the corrosion layer of material *CS*28, the oxygen intensity was higher than that of carbon. More $FeCO_3$ and/or hydroxides such as $Fe(OH)_2$ were likely present in the corrosion layer than Fe_3C. This observation is in accordance with the *XPS* results for the O 1*s* and Fe 2*p* regions for each material shown in Table 5 and Table 6, respectively, where the intensity of $FeCO_3$ or Fe^{2+} decreases with increasing carbon content in the materials. To explain this trend, it should be noted that the micro-galvanic corrosion due to the contact between cementite and ferrite was low in material *CS*28 owing to its low cementite fraction, and also in material *CS*62 because of the small contact area between the spherical-shaped cementite and ferrite phase [75]. The high micro-galvanic corrosion in the pearlitic microstructures (materials *CS*65 and *CS*83) was accompanied by high H^+ amounts released between the remaining Fe_3C layers, and led to a lower *pH*. Thus, the conditions for $FeCO_3$ and Fe^{2+} compounds formation were not favorable. Therefore, the $FeCO_3$ and Fe^{2+} compounds intensity was low in pearlitic microstructures that contained high carbon content in this study.

4.1.3. Corrosion layer morphology and thickness

The sample surface/corrosion layer and the corrosion layer/embedding material interfaces (green and red lines, respectively) in material *CS*28 were more uneven and have a rough appearance compared to the other materials (Fig. 6, left column). To explain this difference, the process of corrosion layer formation was considered. In the CO_2 environment, the $FeCO_3$ precipitation process on the carbon steel surface consisted of two steps: nucleation and growth [76]. In the first step, nucleation occurs near the steel surface or in the solution. After nucleation, the $FeCO_3$ grains start to grow, and all Fe^{2+} and CO_3^{2-} ions predominantly participate in the growth process. The nucleation process almost stops at this stage. The original and primary nucleation step can be accelerated if the carbon steel surface has more of the cementite phase, which can provide some points on the surface for ferrous and carbonate ions to nucleate [77,78]. Hence, the high fraction of the cementite phase in materials *CS*62, *CS*65, and *CS*83 provided more nucleation sites for $FeCO_3$ precipitation than material *CS*28. However, the high corrosion rates in materials *CS*62, *CS*65 and *CS*83 led to a high release of Fe^{2+} from the carbon steel surface, which caused a higher nucleation rate. Therefore, it can be inferred that the nucleation rates in materials *CS*62, *CS*65, and *CS*83, were high, and which may have affected the growth rate and caused the precipitation of small particles of $FeCO_3$ [76,79]. The points and areas that can provide favorable nucleation sites on the surface were few in material *CS*28 because of its low cementite phase fraction and therefore, lowered induced nucleation. Consequently, the growth step was more dominant in this material, which created large particles of $FeCO_3$ and large spaces between the $FeCO_3$ particles [76]. The spaces between the $FeCO_3$ particles provided direct contact between the sample surface and solution, resulting in an accelerated Fe dissolution rate and localized corrosion, which gave rise to a bumpy sample surface/corrosion layer interface (green line). The high concentrations of Fe^{2+} and HCO_3^- ions in the localized corrosion areas between the large carbonate grains led to the precipitation of $FeCO_3$ in these areas, and the large spaces between the first precipitated $FeCO_3$ particles were filled [16,80]. The outcome was the rough sample surface/corrosion layer and the consequent corrosion layer/embedding material interfaces in material *CS*28, can be observed in Fig. 6 (green and red lines) (*CS*28) in the CO_2 environment.

The *SEM* images in Fig. 6 show that the thickness of the corrosion layers increased as the carbon content increased. The only exception is material *CS*65 which shows a slightly lower thickness than material *CS*62. The difference between the corrosion layer thicknesses of these two materials is only 2 μm. Because these thicknesses are the average values measured from the two samples for each material, the 2 μm difference can be ignored. However, this difference may be worth being considering in this study because the same trend in the corrosion layer thicknesses was observed in the CO_2/H_2S environment (Fig. 6(right column)). This means that the corrosion layer thickness of material *CS*65 was lower than that of material *CS*62 in both the CO_2 and the CO_2/H_2S environments. The general thickness increase with carbon content in this study can be attributed to the high Fe^{2+} concentration on the surface of the materials with high carbon content, and consequently the increasing corrosion layer accumulation rate with the increase in carbon content, as shown in Fig. 13. In addition, as it can be seen in Fig. 2 which shows the microstructure of the materials, the cementite phase in material *CS*62 is broken lamella or spheroidite, whereas the cementite morphology in materials *CS*65 and *CS*83 is

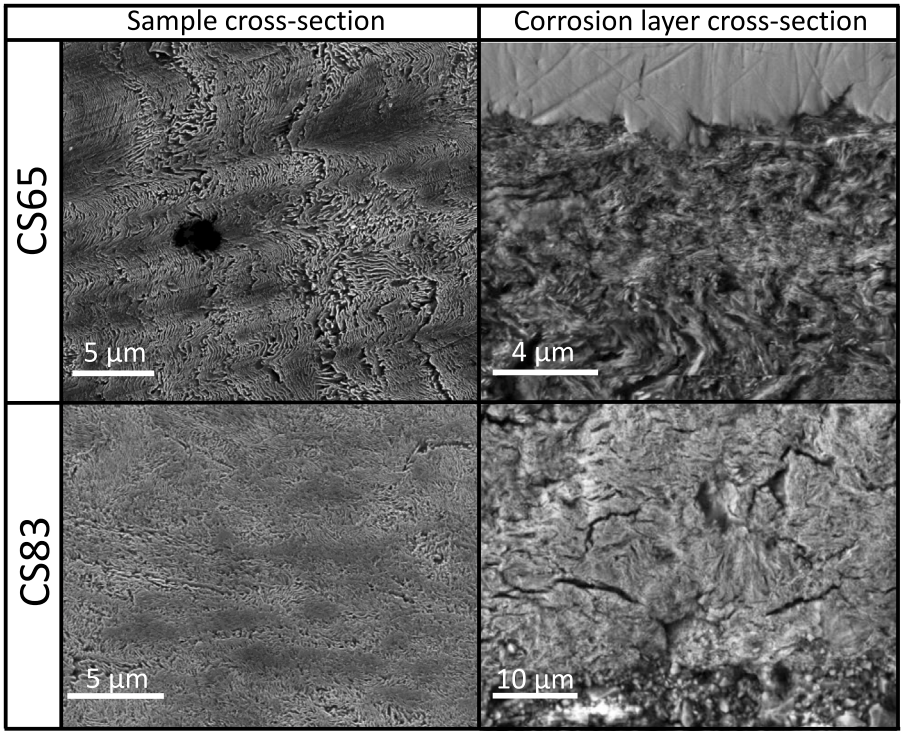

Fig. 12. *SEM* micrographs which show the resemblance of cross-sectional morphologies of the sample microstructure (left column) and the corrosion layer formed on materials *CS*65 and *CS*83 (right column) in the 0.2 bar CO_2 environment.

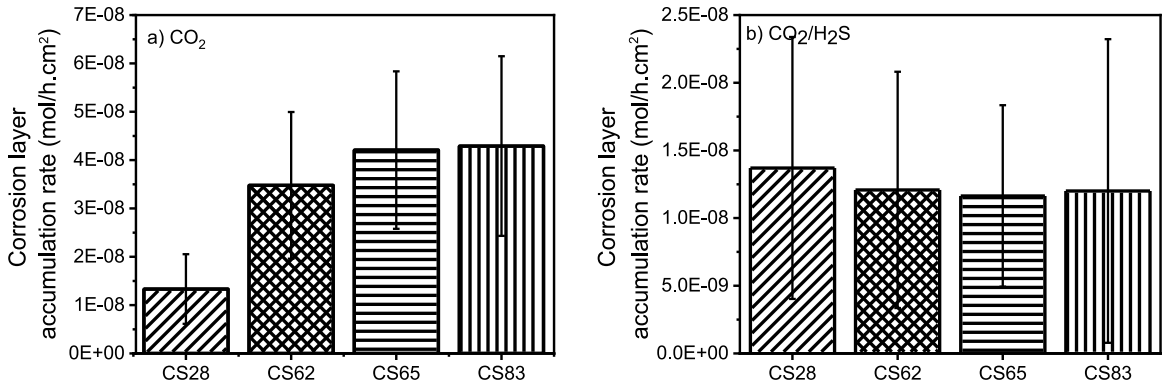

Fig. 13. Corrosion layer accumulation rate for the materials exposed to (a) the 0.2 bar CO_2 environment and (b) the 0.2 bar CO_2/1 mbar H_2S environment for 21 d, respectively. (The columns show the mean value of three tests and the bars represent the standard deviation of the mean value.)

lamellar. These two materials, *CS*65 and *CS*83, had a denser cementite network, which consequently provided more connectable ground for the corrosion products to adhere to the surface and protect it from mechanical breakdown. However, as discussed earlier, the corrosion layer in material *CS*65 was slightly thinner than that in material *CS*62, despite its high corrosion rate and lamellar microstructure. Although material *CS*65 had a lamellar cementite morphology, its microstructure showed that the ferrite areas were larger and connected, whereas small and disconnected ferrite grains constituted the ferritic areas in material *CS*62. A group of small ferrite grains was surrounded by ferrite/cementite grains, and this pattern was repeated throughout the material (Fig. 2). Therefore, material *CS*62 had a more uniform microstructure, which consequently provided a more uniform linking substrate for corrosion products during the corrosion process. In material *CS*65, the connected and big ferrite grains hampered the formation of a uniform remaining Fe_3C network for corrosion product attachment in this material. Consequently, the corrosion layer thickness in this material was lower than that of material *CS*62.

In general, under these study conditions, it seems that the corrosion layers formed in the CO_2 environment were not sufficiently protective to prevent further corrosion; therefore, the high corrosion layer thickness in high-carbon steels did not prevent the corrosion process. Material *CS*28, with the lowest corrosion rate, demonstrated the thinnest layer, whereas the thickest corrosion layer was formed on material *CS*83 which had the highest corrosion rate.

4.1.4. Corrosion layer porosity

Another characteristic of a corrosion layer that can affect the corrosion rate is porosity. As can be observed from the *SEM* images in Fig. 6 (left column), the corrosion layer cross-sections of materials *CS*65 and *CS*83 with the pearlitic microstructure show more porosity than the corrosion layer cross-section of materials *CS*62 and *CS*28. To obtain a clearer image of the corrosion layers porosity, the cross-sections of the corrosion layers of materials *CS*28, *CS*65 and *CS*83, were cut in *FIB* by gallium ions. Based on the *FIB- SEM* images shown in Fig. 11a, material *CS*28 exhibits a compact corrosion layer, whereas materials

*CS*65 and *CS*83 with pearlitic microstructures show porosity in their corrosion layers.

The porous layer formed on materials *CS*65 and *CS*83 with a pearlitic microstructure shown in Fig. 11b and c consist of the remaining Fe_3C lamellae. The hollow spaces between the remaining Fe_3C lamellae are filled with corrosion products in some areas, but there is still a large fraction of hollow spaces between the remaining lamellae, which gives rise to a porous film. There is a resemblance between the corrosion layer morphology and the cross-sectional microstructure of the bare samples in materials *CS*65 and *CS*83 with lamellar microstructures, as shown in Fig. 12. This resemblance clearly shows that the Fe_3C layers remained on the steel surface after the mid-ferrite phases were dissolved, and the corrosion layer adopted almost the same morphology as the original material microstructures. Therefore, the high porosity observed in the corrosion layer of materials *CS*65 and *CS*83 was due to their lamellar microstructure and the presence of remaining Fe_3C in the corrosion layer, as well as the spaces between the remaining Fe_3C layers not being completely filled with corrosion products due to the low Fe^{2+} concentration in the bulk solution in this study. A porous corrosion layer cannot effectively prohibit the permeation of ions at solution [81]. The *LPR* corrosion rate curves in Fig. 3a shows that the corrosion rates increase continuously with time for all materials, and the curve gradient increases with the corrosion layer porosity. That is, the corrosion rate increases faster for materials *CS*65 and *CS*83 which presented more porosity in their corrosion layers, than for materials *CS*28 and *CS*62.

During the first stages of corrosion, when the uncovered sample surface was in contact with the CO_2-containing solution, the micro-galvanic couple of Fe and Fe_3C, and consequently, the remaining Fe_3C, lead to the formation of a corrosion layer that grew with a similar morphology and structure as the sample microstructure. As Crolet et al. [82,83] noted, after the first stage of corrosion, an empty Fe_3C formed and internal acidification due to micro-galvanic coupling impeded the precipitation of $FeCO_3$ in contact with the carbon steel surface. In this case, the corrosion layer was not protective even if the outer layer was obstructed [84]. The unprotective Fe_3C + corrosion product layer is shown in Fig. 11b and c for materials *CS*65 and *CS*83, respectively. However, in material *CS*65 this layer was more porous in the vicinity of the carbon steel surface because the acidification prevents the corrosion product precipitation in this region. At a further distance from the interface, the remaining cementite layers were partially filled with corrosion product, and far from the top of the corrosion layer, Fe^{2+} and Fe^{3+} compounds covered the surface. However, in material *CS*83, the small interlamellar spaces compared with material *CS*65 (Table 3) gave rise to more hydrogen occlusion [85]. Because the H^+ ions can hamper the corrosion product precipitation by decreasing the *pH* [86–89], the unfilled pores and hollow spaces between the remaining Fe_3C layers can be observed all over the corrosion layer cross-section. Hence, the appearance of the cross-sectional morphology and porosity of the corrosion layer was more uniform compared to material *CS*65.

4.2. Proposed mechanisms for the corrosion layer formation in CO_2 environment

A schematic is shown in Fig. 14 to clarify the cementite morphology role in the corrosion layer formation mechanism in the studied materials. As mentioned previously, material *CS*28 with dispersed spherical cementite offered few favorable sites on the surface for $FeCO_3$ nucleation, and the low $FeCO_3$ nucleation rate resulted in the formation of large $FeCO_3$ grains and large spaces between them (Fig. 14 *CS*28 (a) and (b)). The sample surface between the $FeCO_3$ grains corroded at a higher rate than that at the other sites. The resultant high Fe^{2+} concentration in these corroded areas led to the formation of $FeCO_3$, which filled the spaces between the first precipitated $FeCO_3$ layers. The result was a rough metal surface/corrosion layer interface, and the consequent rough corrosion layer/embedding material interface (Fig. 14 *CS*28 (c) and Fig. 6).

In material *CS*62, the uniform microstructure was due to the spherical and broken lamella cementite particles, which were evenly distributed throughout the material, and the repeated surrounding ferrite regions which were several microns in size. As shown in the schematic in Fig. 14 *CS*62 (a), this microstructure provided more sites for $FeCO_3$ nucleation. The micro-galvanic effect between cementite and ferrite caused ferrite phase dissolution. Because the cementite phase consisted of spherical and broken lamella, dissolution of the ferrite phase caused the cementite phase to be released and dissolved into the electrolyte. Only a small fraction of cementite remained on the surface, and corrosion product formed between the remaining cementite Fig. 14 *CS*62 (b). It has been previously mentioned that the corrosion layer formed in the CO_2 environment showed an inefficient protectiveness and, therefore, the sample surface corroded continuously during the test. This gave rise to a porous corrosion layer. At a distance from the metal surface towards the corrosion layer and electrolyte interface, a compact layer of $FeCO_3$ formed (Fig. 14 *CS*62 (c)).

The microstructure of material *CS*65 consisted of lamellar cementite phase and connected ferrite regions. Two distinct features in this material microstructure contributed to the morphology, thickness, and surface roughness of the corrosion layer formation: pearlite colonies and a connected ferrite phase. As discussed, the ferrite regions are favorable places for corrosion and dissolution sooner than the pearlite regions. This resulted in the formation of a non-uniform and uneven corroded surface, as shown in Fig. 14 *CS*65 (b). This can lead to the break down of the remaining Fe_3C and formed $FeCO_3$, which caused the formation of a rough corrosion layer, Fig. 14 *CS*65 (c).

Material *CS*83 had the highest carbon content and cementite fraction among the studied materials. The pearlite colonies with very small and confined ferrite regions constituted the material *CS*83 microstructure, and its interlamellar spacing was lower than of material *CS*65 (Fig. 14 *CS*83 (a) and Table 3). Material *CS*83 exhibited a more uniform microstructure than material *CS*65. The micro-galvanic effect between ferrite and cementite led to the dissolution of ferrite and a connected stable network of the remaining Fe_3C in the formed corrosion layer. The high micro-galvanic corrosion owing to the high cementite fraction in this material was accompanied by a high H^+ release, which led to a low *pH* and high acidity between the remaining Fe_3C layers. In addition, the small interlamellar spacing, which led to a slow process of hydrogen ion diffusion from the interlamellar spaces towards the electrolyte, gave rise to high acidity at this material surface. This resultant acidity was not a favorable condition for corrosion product formation, and the high porosity was the result of incomplete coverage of corrosion product between the Fe_3C layers (Fig. 14 *CS*83 (b) and (c)). A compact corrosion layer of $FeCO_3$ was formed on top of the corrosion layer/electrolyte interface.

4.3. CO_2/H_2S environment

The corrosion behavior of carbon steels in H_2S-containing solutions has been extensively studied, and the results revealed that H_2S accelerates both anodic iron dissolution and cathodic hydrogen evolution in most cases [6,18,39,90–96]. However, it has been reported that under low concentrations of H_2S (up to approximately 0.908 mbar) and special conditions (*pH* range of 3–5, and long exposure time, i.e., 2 h or more), H_2S has a strong inhibiting effect on the corrosion of iron [18,97,98]. As is shown in Fig. 3b, the addition of 1 mbar H_2S induced a significant reduction in the corrosion rate by one order of magnitude compared to the CO_2 environment. This retardation was first mentioned by Shoesmith et al. [99] as the effect of the very rapid formation of a thin FeS_{ads} film in a solid-state process by the direct reaction of H_2S and Fe. This film can displace the adsorbed H_2O and OH^- from the carbon steel surface and affect the surface double layer [100], which in turn slows the kinetics of the electrochemical reactions including

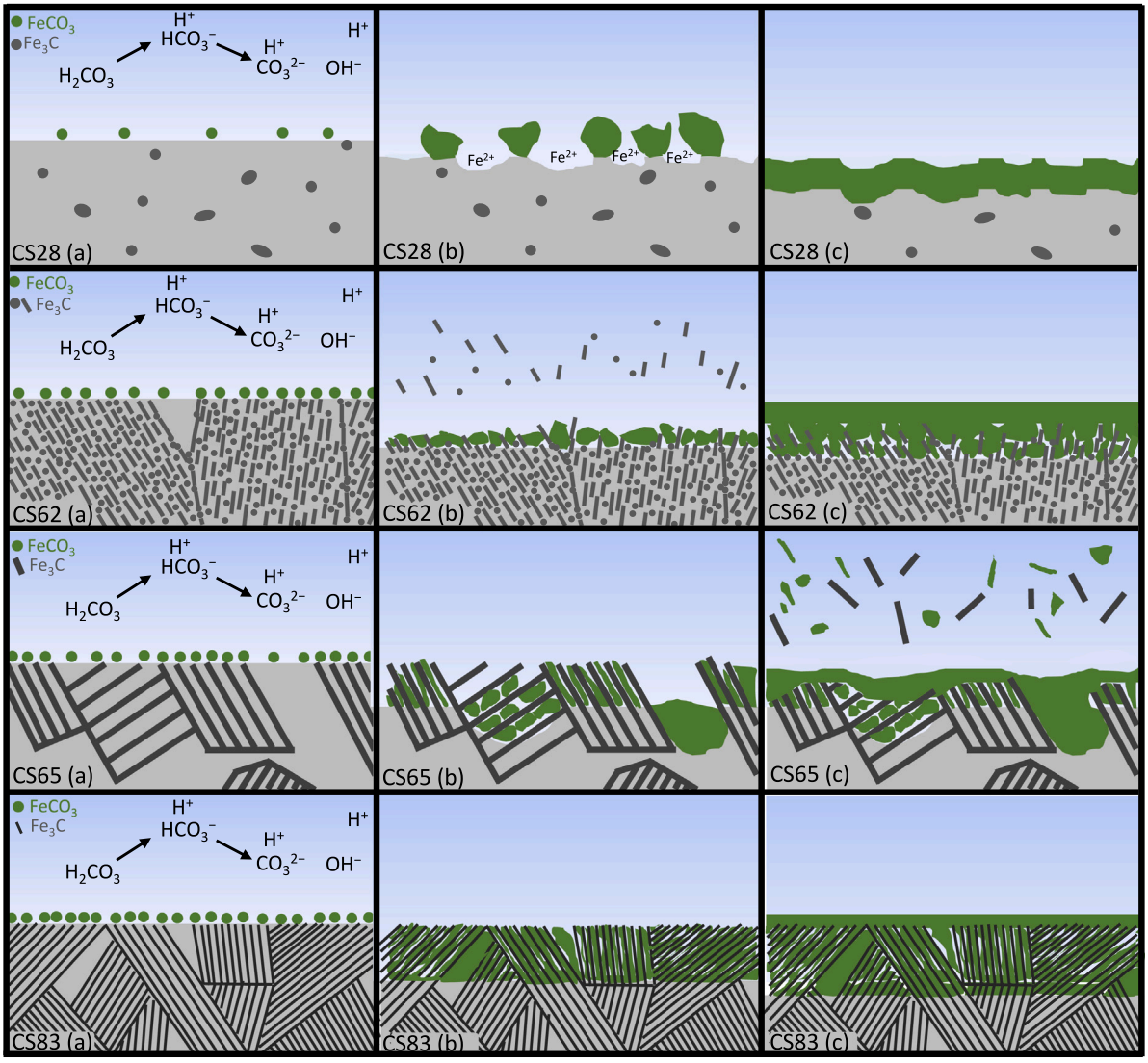

Fig. 14. Schematic representations of the evolution mechanism of $FeCO_3$ corrosion layer in the 0.2 bar CO_2 environment for all materials.

anodic Fe dissolution, H_2O reduction (by an order of magnitude), and HCO_3^- reduction (by a factor of 3) [101].

Previous studies have shown that as long as thermodynamics permit, by considering the kinetics formation of different FeS phases, the initial phase that forms on the carbon steel surface in a CO_2/H_2S environment is mackinawite (FeS) in a direct solid-state reaction between H_2S and the carbon steel surface [102–104]. The carbon steel surface reacts with the dissolved H_2S and $FeHS^+_{ads}$ is formed on the surface. This ion directly participates in making the mackinawite film (*eq*.9) [99,105]. $FeHS^+_{ads}$ can also migrate from the carbon steel surface towards the solution. The formation rate of mackinawite is much faster than $FeHS^+_{ads}$ migration and dissolution, and it can be formed even when the bulk solution is under the saturation level [106]. Pessu et al. [107] showed that the corrosion potential increases quickly at 1000 *ppm* of H_2S compared with high H_2S concentrations (10000 and 1000000 *ppm*) in a CO_2/H_2S mixed solution, whereas after 60 *h*, it starts to decrease towards a more negative potential. They concluded that a fast process of iron sulfide formation occurred on the carbon steel surface at low H_2S concentration (1000 *ppm*, which is almost the same as the H_2S concentration used in the present study). As mentioned previously, the immediate drop in the *LPR* corrosion rates in Fig. 3b can be attributed to the fast formation of the FeS layer at a low concentration of H_2S used in the present study. According to Woollam et al. [71] who investigated the effect of various parameters on a thermodynamically stable film in the presence of CO_2 and H_2S, the formation of mackinawite is favored under the present study test conditions. $FeCO_3$ does not have the same formation kinetics as mackinawite, but can be formed within the mackinawite layer through the diffusion of H_2CO_3. Because H_2S reacts very quickly with Fe^{2+} ions diffusing from the carbon steel surface towards the solution, it is not expected that H_2S will diffuse through the developing layer. However, H_2CO_3 which is slow to react, can diffuse through the layer and react with Fe^{2+} ions to form $FeCO_3$ or other Fe^{2+} compounds [108]. As discussed in the previous section, the Fe_3C residues on the corroding carbon steel surface can significantly improve the mechanical attachment of the corrosion product to the metal surface. Bonaventura et al. [109] showed that even $FeCO_3$ formation could be prevented if the remaining Fe_3C layer is damaged. Therefore, because of the significant decrease in the corrosion rate in the presence of H_2S and the fast formation of the FeS layer, the corrosion process does not leave a large amount of Fe_3C on the surface, which consequently leads to a substantial reduction in the corrosion layer thickness in comparison with the layer thicknesses in the CO_2 environment (Fig. 6).

The *XPS* results (Fig. 9) confirm the formation of two iron sulfides which are FeS (mackinawite) and FeS_2 (pyrite) and Fe^{2+} and Fe^{3+} compounds, such as iron oxide (Fe_2O_3) in the CO_2/H_2S environment in

the corrosion layers of all the studied materials. Based on the relative intensities in Table 7, it can be seen that the iron sulfides intensities in pearlitic microstructures (materials *CS*65 and *CS*83) are high, whereas the sum of Fe^{2+} and Fe^{3+} compounds is higher in the corrosion layers of materials *CS*28 and *CS*62. Because mackinawite and pyrite form a more protective surface layer [110], the corrosion rates of materials *CS*65 and *CS*83, which have layers rich in iron sulfide species, are low in the CO_2/H_2S environment (during the initial hours of exposure for material *CS*65, and until the end of the exposure for material *CS*83). Material *CS*65 showed a slightly higher intensity of iron sulfide species than material *CS*83; however, it showed a higher corrosion rate and a continuous increase in the corrosion rate during the test. The role of the microstructure on the corrosion layer morphology and thickness, which in turn results in its unusual corrosion behavior, will be discussed in the following paragraphs. This behavior is discussed here from the perspective of the corrosion layer composition. As observable in Table 7, the relative intensity of pyrite is 29.2 and 15.7 in materials *CS*65 and *CS*83, respectively. The formation of pyrite is accompanied by the evolution of hydrogen, as identified using mass spectroscopy by Taylor et al. [111]. Hydrogen can be produced as follows:

$$FeS + H_2S \rightarrow FeS_2 + H_2 \quad (16)$$

In fact, pyrite formation on steels in an aqueous H_2S solution produces disulfide anions at the anodic sites and hydrogen at the cathodic sites [112,113]. As such, the reaction between the generated S_2^{2-} and dissolved Fe^{2+} leads to the crystallization of pyrite at the anodic sites [111]:

$$2HS^- \rightarrow S_2^{2-} + 2H^+ + 2e^- \quad (17)$$

$$2H^+ + 2e^- \rightarrow H_2 \quad (18)$$

$$Fe^{2+} + S_2^{2-} \rightarrow FeS_2 \quad (19)$$

The formation mechanism of pyrite which is accompanied by a cathodic reaction, can boost the corrosion rate [114]; therefore, the high relative intensity of pyrite in material *CS*65 in comparison with material *CS*83 can be a reason for its high and increased corrosion rate. Rickard [115] indicated that pyrite generally forms approximately after one week. The *LPR* curve of material *CS*65 in Fig. 3b shows a small change in the gradient at approximately 152 *h* (almost one week). After this point, the corrosion rate rises at an increased rate, which can be attributed to the formation of pyrite in this material. The pyrite proportion in the other studied materials was not sufficiently high to cause a change in the corrosion rate gradient.

According to Fig. 3b, the corrosion layer formed in the CO_2/H_2S solution shows better protection characteristics than the layer formed in the CO_2 environment. The *LPR* corrosion rate curves show that the corrosion layer formed on material *CS*28 reaches its peak protectiveness after 80 h, whereas the peak protectiveness is obtained after 57, 54, and 41 h, for materials *CS*62, *CS*65, and *CS*83, respectively. This trend shows that the corrosion layer protectiveness increased with an increase in the carbon content and cementite phase fraction. After the maximum protectiveness was reached, the corrosion rate stabilized for material *CS*28, whereas there was a slight increase in the corrosion rates of materials *CS*62 and *CS*83, and an increased increment was observed for material *CS*65 (Fig. 3b). The corrosion rates in materials *CS*62 and *CS*65 were the same between 85 and 152 h, however after that, material *CS*65 exhibited a considerably higher corrosion rate than material *CS*62. Because the carbon content and the cementite fraction were very close in materials *CS*62 and *CS*65, it can be inferred that the carbon steel microstructure was a pertinent factor in controlling the corrosion rate and corrosion layer protectiveness. Anyanwu et al. [37] reported the preferential development of an iron sulfide layer above pearlite regions in a ferritic/pearlitic microstructure. They showed that a thin and continuous layer of iron sulfide, which was formed on the pure iron material in the CO_2/H_2S environment with 0.1 bar H_2S was loosely attached in comparison with the iron sulfide layer formed on the ferrite/pearlite sample. Bai et al. [116] reported a high precipitation rate of the iron sulfide layer on the pearlite regions in a ferrite/pearlite microstructure exposed to an H_2S environment. Their studies showed that the iron sulfide layer formed on the ferrite/pearlite microstructure was more protective than the layer formed on a bainitic microstructure. In the H_2S environment, hydrogen ion (H^+) reduction and hydrogen sulfide reduction reactions occurred in the cementite phase as cathodic reactions, owing to the local micro-galvanic cell between the ferrite and cementite in the pearlitic microstructure. These cathodic reactions caused a decrease in the hydrogen ion concentration. The high iron dissolution in the ferrite phase, along with the reduced hydrogen ion concentration and the consequently raised pH, generated favorable conditions for iron sulfide formation above the pearlite regions. Furthermore, the presence of the remaining iron carbide, notwithstanding its low amount, promoted the structural attachment of the iron sulfide layer. Despite the pearlitic microstructure of material *CS*65, it showed a higher corrosion rate than material *CS*62 with a spheroidite microstructure. Kim et al. [34] investigated the effects of the pearlitic and bainitic microstructures on sulfide scale formation. They concluded that the distance from ferrite to cementite, which was 10 μm in the pearlite/ferrite microstructure, could lead to a high *pH* gradient on the surface of the sample, whereas it was unlikely for a bainite microstructure with few μm or less between ferrite and cementite, resulting in *pH* gradient. In the studied materials with pearlitic microstructures, *CS*65 and *CS*83, the lamellar spaces were at the nanoscale; therefore, we can consider that when the *pH* above the cementite phase increases, the entire pearlitic area experiences an increased *pH*. In the microstructures of these two materials, there are pure ferrite grains between the pearlite colonies, which can also cause a *pH* gradient. In material *CS*83, the size of the ferritic grains between the ferrite/cementite colonies was a few μm (less than 10 μm), and the *pH* gradient formation was improbable. In material *CS*65, the ferrite grain size was approximately 10 μm or more, and the *pH* gradient that occurred on the material surface resulted in the formation of an uneven iron sulfide film. Moreover, the connected ferrite grains impeded the formation of a uniform remaining Fe_3C structure for iron sulfide attachment in this material. In Fig. 15, a hollow space within the remaining Fe_3C network is marked on the corrosion layer of the material *CS*65. This discontinuity is observed less in materials *CS*83 and *CS*62. The uniform cementite dispersion on these two materials provided a more uniform Fe_3C structural base for the attachment of the protective iron sulfide film. Therefore, material *CS*65 exhibited a higher corrosion rate (Fig. 3b and Fig. 4b).

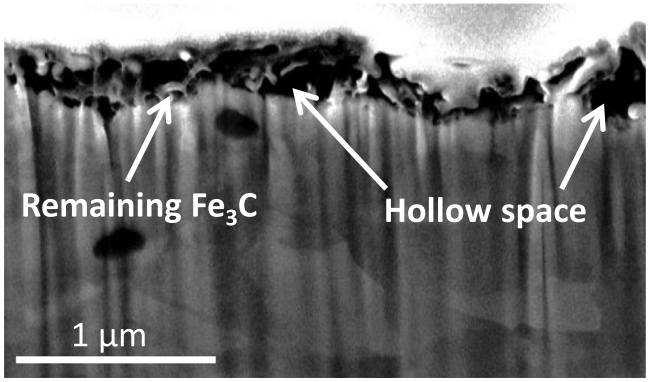

Fig. 15. *SEM* micrograph of the morphology of the corrosion layer formed on material *CS*65 in the 0.2 bar CO_2/1 mbar H_2S environment.

According to Fig. 6, material *CS*28, with the lowest carbon content, displays the thinnest corrosion layer among the studied materials. This

material had the lowest fraction of Fe_3C. However, Fig. 13b shows that all materials have almost identical corrosion layer accumulation rate, considering the large error bars. This implies that the corrosion layer formed on material $CS28$ was more compact than that on other materials, whereas the loose attachment of the corrosion layer of this material to the metal substrate, owing to the less connected Fe_3C network, can be a reason for its low thickness. The other three high-carbon steel materials, $CS62$, $CS65$, and $CS83$, exhibited a porous corrosion layer because of the presence of the remaining Fe_3C in the layer.

5. Conclusions

Corrosion tests in the modified $ASTM\ D1141$-90 electrolyte in the 0.2 bar CO_2 and 0.2 bar CO_2/1 mbar H_2S environments were performed on four carbon steels with different microstructures for 21 d. After exposure, the corrosion layers were characterized with $SEM-EDS$, FIB, and XPS to reveal the effect of microstructures on layer formation and the corresponding corrosion properties. The results revealed the following:

- The corrosion layer formed on all materials in the CO_2/H_2S environment provided significant protection, in contrast to the layer formed in the CO_2 environment.
- By comparing the behavior of different carbon steels, it can be observed that with increasing carbon content and cementite phase fraction, the corrosion rate increased in the CO_2 environment while no special trend was observed in the CO_2/H_2S environment.
- Despite the thick corrosion layers formed on materials with high carbon content and cementite fraction in the CO_2 environment, their protectivity was insufficient to prevent the high corrosion rates which were escalated by the micro-galvanic effect. This was due to the high porosity observed in their corrosion layers. The corrosion rate of the material $CS65$ with a ferritic/pearlitic microstructure was higher than the material $CS62$ with a spheroidite microstructure owing to the more prominent micro-galvanic effect in lamellar microstructures.
- After the materials in the CO_2/H_2S environment reached their maximum protectiveness, the corrosion rate of material $CS28$ with the lowest carbon content, stabilized, while there was a slight increase in the corrosion rates for materials $CS62$ (spheroidite microstructure) and $CS83$ (lamellar microstructure). The material $CS65$ (lamellar microstructure with connected ferrite phase) demonstrated a high increase until the end of the test. The higher proportion of pyrite in the corrosion layer of the material $CS65$ in comparison with other materials can be a reason for the higher corrosion rate experienced by this material in the CO_2/H_2S environment.
- In the CO_2 environment, the corrosion layers contained the remaining Fe_3C, and the porosity between the Fe_3C layers or particles was partially filled by the corrosion products. EDS analysis showed the presence of iron, carbon and oxygen elements in the corrosion products.
- The XPS analysis of the top surface of corrosion layers indicated that all corrosion products in both environments contained Fe^{2+} and Fe^{3+} related compounds such as ferric oxide regardless of their microstructures.
- It was found from XPS results that increasing the carbon content, particularly in ferritic/pearlitic microstructures, the proportions of Fe^{2+} compounds decreased and the proportions of the Fe^{3+} related compounds increased.

CRediT authorship contribution statement

Shabnam Karimi: Conceptualization, Data curation, Investigation, Methodology, Visualization, Writing – original draft, Writing – review & editing. **Iman Taji:** Conceptualization, Data curation, Investigation, Methodology, Writing – review & editing. **Tarlan Hajilou:** Conceptualization, Data curation, Investigation, Methodology, Writing – review & editing. **Simona Palencsár:** Conceptualization, Data curation, Investigation, Methodology, Writing – review & editing. **Arne Dugstad:** Conceptualization, Data curation, Investigation, Methodology, Writing – review & editing. **Afrooz Barnoush:** Funding acquisition, Supervision, Writing – review & editing. **Kim Verbeken:** Supervision, Writing – review & editing. **Tom Depover:** Supervision, Writing – review & editing. **Roy Johnsen:** Conceptualization, Funding acquisition, Supervision, Writing – review & editing.

Declaration of competing interest

The authors declare the following financial interests/personal relationships which may be considered as potential competing interests: Shabnam Karimi reports financial support was provided by Norwegian University of Science and Technology.

Data availability

Data will be made available on request.

Acknowledgments

This work was performed as part of the KPN project "Environmental Cracking of Flexible Pipe Armour Wires", Research Council of Norway project no. 280760 within the $PETROMAKS$ 2 program. The authors would like to thank the following project participants for financial and technical support: The Research Council of Norway, Equinor, Norway, Shell, Chevron, Petrobras, Norway, *OKEA*, Norway, Technip*FMC*, *NOV*, Baker Hughes, Norway and 4Subsea, Norway.

References

[1] Y. Bai, Q. Bai, Subsea Pipelines and Risers, Elsevier, 2005.
[2] A. Rubin, S. Overby, T.S. Nielsen, M.H. Haarh, J. Gudme, Corrosion rates of carbon steel in confined environments, in: Corrosion 2012, OnePetro, 2012.
[3] C. Taravel-Condat, N. Desamais, Qualification of high strength carbon steel wires for use in specific annulus environment of flexible pipes containing CO_2 and H_2S, in: International Conference on Offshore Mechanics and Arctic Engineering, Vol. 47489, 2006, pp. 585–591.
[4] P.C. Singer, W. Stumm, The solubility of ferrous iron in carbonate-bearing waters, J.-Am. Water Works Assoc. 62 (3) (1970) 198–202.
[5] I. Shabalov, Y. Matrosov, A. Kholodnyi, M. Matrosov, V. Velikodnev, Effect of hydrogen sulfide-containing media on pipe steels, in: Pipeline Steels for Sour Service, Springer, 2019, pp. 1–28.
[6] H. Vedage, T.A. Ramanarayanan, J. Mumford, S. Smith, Electrochemical growth of iron sulfide films in H_2S-saturated chloride media, Corrosion 49 (2) (1993) 114–121.
[7] W. Liu, S.-L. Lu, Y. Zhang, Z.-C. Fang, X.-M. Wang, M.-X. Lu, Corrosion performance of 3% Cr steel in CO_2-H_2S environment compared with carbon steel, Mater. Corros. 66 (11) (2015) 1232–1244.
[8] Y. Wang, B. Wang, S. He, L. Zhang, X. Xing, H. Li, M. Lu, Unraveling the effect of H_2S on the corrosion behavior of high strength sulfur-resistant steel in $CO_2/H_2S/Cl$- environments at ultra high temperature and high pressure, J. Nat. Gas Sci. Eng. (2022) 104477.
[9] J. Hesketh, E. Dickinson, M. Martin, G. Hinds, A. Turnbull, Influence of H_2S on the pitting corrosion of 316L stainless steel in oilfield brine, Corros. Sci. 182 (2021) 109265.
[10] J. Sardisco, W.B. Wright, E. Greco, Corrosion of iron in on H_2S-CO_2-H_2O system: corrosion film properties on pure iron, Corrosion 19 (10) (1963) 354t–359t.
[11] T. Murata, R. Matsuhashi, T. Taniguchi, K. Yamamoto, The evaluation of H_2S containing environments from the viewpoint of OCTG and linepipe for sour gas applications, in: Offshore Technology Conference, OnePetro, 1979.
[12] P. Narayan, J. Anderegg, C. Chen, An ESCA study of Iron Sulfidation in H_2S, J. Electron Spectrosc. Relat. Phenom. 27 (3) (1982) 233–242.

[13] S. Smith, E. Wright, Prediction of minimum H_2S levels required for slightly sour corrosion, Tech. rep., NACE International, Houston, TX (United States), 1994.

[14] R.A. Berner, Stability fields of iron minerals in anaerobic marine sediments, J. Geol. 72 (6) (1964) 826–834.

[15] J. Kvarekval, R. Nyborg, M. Seiersten, Corrosion product films on carbon steel in semi-sour CO_2/H_2S environments, in: CORROSION 2002, OnePetro, 2002.

[16] S. Zhang, Y. Li, B. Liu, L. Mou, S. Yu, Y. Zhang, X. Yan, Understanding the synergistic effect of CO_2, H_2S and fluid flow towards carbon steel corrosion, Vacuum 196 (2022) 110790.

[17] P. Sui, C. Sun, Y. Hua, J. Sun, Y. Wang, The influence of flow rate on corrosion behavior of $X65$ carbon steel in water-saturated supercritical CO_2/H_2S system, in: CORROSION 2019, OnePetro, 2019.

[18] J. Sardisco, R. Pitts, Corrosion of iron in an H_2S-CO_2-H_2O system composition and protectiveness of the sulfide film as a function off pH, Corrosion 21 (11) (1965) 350–354.

[19] W.F. Rogers, A. Rowe, 3. Corrosion effects of hydrogen sulphide and carbon dioxide in oil production, in: 4th World Petroleum Congress, OnePetro, 1955.

[20] S.P. Ewing, Electrochemical studies of the hydrogen sulfide corrosion mechanism, Corrosion 11 (11) (1955) 51–55.

[21] E. Abelev, J. Sellberg, T. Ramanarayanan, S. Bernasek, Effect of H_2S on Fe corrosion in CO_2-saturated brine, J. Mater. Sci. 44 (22) (2009) 6167–6181.

[22] F. Shi, L. Zhang, J. Yang, M. Lu, J. Ding, H. Li, Polymorphous FeS corrosion products of pipeline steel under highly sour conditions, Corros. Sci. 102 (2016) 103–113.

[23] R. Souza, B. Santos, M. Gonçalves, E.M. Júnior, T. Simões, J. Oliveira, G. Vaz, L. Caldeira, J. Gomes, A. Bueno, The role of temperature and H_2S (thiosulfate) on the corrosion products of API $X65$ carbon steel exposed to sweet environment, J. Pet. Sci. Eng. 180 (2019) 78–88.

[24] R. Elgaddafi, A. Naidu, R. Ahmed, S. Shah, S. Hassani, S.O. Osisanya, A. Saasen, Modeling and experimental study of CO_2 corrosion on carbon steel at elevated pressure and temperature, J. Nat. Gas Sci. Eng. 27 (2015) 1620–1629.

[25] B. Pound, G. Wright, R. Sharp, The anodic behavior of iron in hydrogen sulfide solutions, Corrosion 45 (5) (1989) 386–392.

[26] D.W. Shannon, Role of chemical components in geothermal brine on corrosion, CORROSION/78, Paper (57) (1978).

[27] C. Ding, K.-w. Gao, C.-f. Chen, Effect of Ca^{2+} on CO_2 corrosion properties of $X65$ pipeline steel, Int. J. Miner. Metall. Mater. 16 (6) (2009) 661–666.

[28] Z. Wang, L. Zhang, Z. Zhang, M. Lu, Combined effect of pH and H2S on the structure of passive film formed on type 316L stainless steel, Appl. Surf. Sci. 458 (2018) 686–699.

[29] S.J. Kim, H.G. Jung, G.T. Park, K.Y. Kim, Effect of Cu and Ni on sulfide film formation and corrosion behavior of pressure vessel steel in acid sour environment, Appl. Surf. Sci. 313 (2014) 396–404.

[30] S. Koh, J. Lee, B. Yang, K. Kim, Effect of molybdenum and chromium addition on the susceptibility to sulfide stress cracking of high-strength, low-alloy steels, Corrosion 63 (3) (2007) 220–230.

[31] H. Inagaki, M. Tanimura, I. Matsushima, T. Nishimura, Effect of Cu on the hydrogen induced cracking of the pipe line steel, Trans. Iron Steel Inst. Japan 18 (3) (1978) 149–156.

[32] C. Palacios, J. Shadley, Characteristics of corrosion scales on steels in a CO_2-saturated $NaCl$ brine, Corrosion 47 (2) (1991) 122–127.

[33] A. Dugstad, H. Hemmer, M. Seiersten, Effect of steel microstructure on corrosion rate and protective iron carbonate film formation, Corrosion 57 (04) (2001).

[34] S.J. Kim, J.H. Park, K.Y. Kim, Effect of microstructure on sulfide scale formation and corrosion behavior of pressure vessel steel in sour environment, Mater. Charact. 111 (2016) 14–20.

[35] D. Lopez, W.d. Schreiner, S. De Sánchez, S. Simison, The influence of carbon steel microstructure on corrosion layers: an XPS and SEM characterization, Appl. Surf. Sci. 207 (1–4) (2003) 69–85.

[36] M. Ueda, H. Takabe, Effect of environmental factor and microstructure on morphology of corrosion products in CO_2 environments, Tech. rep., NACE International, Houston, TX (United States), 1999.

[37] E. Anyanwu, B. Brown, M. Singer, Effect of iron carbide on the morphology and protectiveness of iron sulfide layer, in: CORROSION 2020, OnePetro, 2020.

[38] F. Farelas, B. Brown, S. Nešić, Iron carbide and its influence on the formation of protective iron carbonate in CO_2 corrosion of mild steel, in: CORROSION 2013, OnePetro, 2013.

[39] H.-H. Huang, W.-T. Tsai, J.-T. Lee, Electrochemical behavior of the simulated heat-affected zone of $A516$ carbon steel in H_2S solution, Electrochim. Acta 41 (7–8) (1996) 1191–1199.

[40] A.M. Zimer, E.C. Rios, P.d.C.D. Mendes, W.N. Gonçalves, O.M. Bruno, E.C. Pereira, L.H. Mascaro, Investigation of $AISI$ 1040 steel corrosion in H_2S solution containing chloride ions by digital image processing coupled with electrochemical techniques, Corros. Sci. 53 (10) (2011) 3193–3201.

[41] E.S. Skilbred, M. Kappes, M. Iannuzzi, R. Johnsen, Hydrogen uptake and diffusivity in steel armor wires with different chemical composition, carbide distribution, grain size, and degree of deformation, Mater. Corros. (2021).

[42] S. Karimi, I. Taji, T. Hajilou, A. Barnoush, R. Johnsen, Evaluation of the cementite morphology influence on the hydrogen induced crack nucleation and propagation path in carbon steels, Int. J. Hydrogen Energy 47 (30) (2022) 14121–14129.

[43] American Society for Testing and Materials, Standard Practice for the Preparation of Substitute Ocean Water, ASTM International, 2013.

[44] S. Navabzadeh Esmaeely, Y.-S. Choi, D. Young, S. Nešić, Effect of calcium on the formation and protectiveness of iron carbonate layer in CO_2 corrosion, Corrosion 69 (9) (2013) 912–920.

[45] M. Stern, A.L. Geary, Electrochemical polarization: I. a theoretical analysis of the shape of polarization curves, J. Electrochem. Soc. 104 (1) (1957) 56.

[46] M. Stern, A method for determining corrosion rates from linear polarization data, Corrosion 14 (9) (1958) 60–64.

[47] G. Astm, Standard test method for conducting potentiodynamic polarization resistance measurements, in: Annual Book of ASTM Standards, Vol. 3, 2009, pp. 237–239.

[48] M. Stern, E. Weisert, Experimental observations on the relation between polarization resistance and corrosion rate, in: Proc. Am. Soc. Test. Mater, vol. 59, 1959, p. 1280.

[49] American Society for Testing and Materials (Filadelfia, Pennsylvania), ASTM G1-03: Standard Practice for Preparing, Cleaning, and Evaluating Corrosion Test Specimens, ASTM, 2004.

[50] C. Sun, Y. Wang, J. Sun, X. Lin, X. Li, H. Liu, X. Cheng, Effect of impurity on the corrosion behavior of X65 steel in water-saturated supercritical CO_2 system, J. Supercrit. Fluids 116 (2016) 70–82.

[51] X. Dou, D. Zhang, B. Li, H. Jing, H. Xu, Electrochemical studies on local corrosion behavior mechanism of super ferrite stainless steel in low-temperature geothermal water environment, in: IOP Conference Series: Materials Science and Engineering, Vol. 493, (1) IOP Publishing, 2019, 012081.

[52] T. Berntsen, M. Seiersten, T. Hemmingsen, Effect of $FeCO_3$ supersaturation and carbide exposure on the CO_2 corrosion rate of carbon steel, Corrosion 69 (6) (2013) 601–613.

[53] A. Dugstad, P.-E. Dronen, Efficient corrosion control of gas condensate pipelines by pH-stabilization, in: CORROSION 99, OnePetro, 1999.

[54] M. Shayegani, M. Ghorbani, A. Afshar, M. Rahmaniyan, Modelling of carbon dioxide corrosion of steel with iron carbonate precipitation, Corros. Eng. Sci. Technol. 44 (2) (2009) 128–136.

[55] J. Chastain, R.C. King Jr., Handbook of X-ray photoelectron spectroscopy, Perkin-Elmer Corporation 40 (1992) 221.

[56] J. Heuer, J. Stubbins, An XPS characterization of $FeCO_3$ films from CO_2 corrosion, Corros. Sci. 41 (7) (1999) 1231–1243.

[57] X. Yue, L. Zhang, Y. Wang, S. Xu, C. Wang, M. Lu, A. Neville, Y. Hua, Evolution and characterization of the film formed on super $13Cr$ stainless steel in CO_2-saturated formation water at high temperature, Corros. Sci. 163 (2020) 108277.

[58] M.C. Biesinger, B.P. Payne, A.P. Grosvenor, L.W. Lau, A.R. Gerson, R.S.C. Smart, Resolving surface chemical states in XPS analysis of first row transition metals, oxides and hydroxides: Cr, Mn, Fe, Co and Ni, Appl. Surf. Sci. 257 (7) (2011) 2717–2730.

[59] M. Rogowska, J. Gudme, A. Rubin, K. Pantleon, R. Ambat, Effect of fe ion concentration on corrosion of carbon steel in CO2 environment, Corros. Eng. Sci. Technol. 51 (1) (2016) 25–36.

[60] G. Carter, J.S. Colligon, Ion Bombardment of Solids, American Elsevier Publishing CO., New York, 1968, p. 446.

[61] K. Wandelt, Photoemission studies of adsorbed oxygen and oxide layers, Surf. Sci. Rep. 2 (1) (1982) 1–121.

[62] R. King, J. Miller, J. Smith, Corrosion of mild steel by iron sulphides, Br. Corros. J. 8 (3) (1973) 137–141.

[63] F. Farelas, M. Galicia, B. Brown, S. Nešić, H. Castaneda, Evolution of dissolution processes at the interface of carbon steel corroding in a CO_2 environment studied by EIS, Corros. Sci. 52 (2) (2010) 509–517.

[64] D. Staicopolus, The role of cementite in the acidic corrosion of steel, J. Electrochem. Soc. 110 (11) (1963) 1121.

[65] K. Videm, J. Kvarekval, T.E. Perez, G. Fitzsimons, Surface effects on the electrochemistry of iron and carbon steel electrodes in aqueous CO_2 solutions, in: CORROSION 96, OnePetro, 1996.

[66] S. Al-Hassan, B. Mishra, D. Olson, M. Salama, Effect of microstructure on corrosion of steels in aqueous solutions containing carbon dioxide, Corrosion 54 (06) (1998).

[67] E. Van Hunnik, E. Hendriksen, B.F. Pots, The formation of protective $FeCO_3$ corrosion product layers in CO_2 corrosion, in: CORROSION 96, OnePetro, 1996.

[68] D. Clover, B. Kinsella, B. Pejcic, R. De Marco, The influence of microstructure on the corrosion rate of various carbon steels, J. Appl. Electrochem. 35 (2) (2005) 139–149.

[69] E. Gulbrandsen, A. Stangeland, T. Burchardt, S. Nešić, S. Morten Hesjevik, S. Skjfrve, B. Sundfer, Effect of precorrosion on the performance of inhibitors for CO_2 corrosion of carbon steel, in: CORROSION 98, OnePetro, 1998.

[70] S. Nešic, M. Nordsveen, R. Nyborg, A. Stangeland, A mechanistic model for carbon dioxide corrosion of mild steel in the presence of protective iron carbonate films—part 2: a numerical experiment, Corrosion 59 (6) (2003) 489–497.

[71] R. Woollam, K. Tummala, J. Vera, S. Hernandez, Thermodynamic prediction of $FeCO_3/FeS$ corrosion product films, in: CORROSION 2011, OnePetro, 2011.

[72] S. Nešić, J. Postlethwaite, S. Olsen, An electrochemical model for prediction of corrosion of mild steel in aqueous carbon dioxide solutions, Corrosion 52 (4) (1996) 280–294.

[73] R. Barker, I. Al Shaaili, R. De Motte, D. Burkle, T. Charpentier, S. Vargas, A. Neville, Iron carbonate formation kinetics onto corroding and pre-filmed carbon steel surfaces in carbon dioxide corrosion environments, Appl. Surf. Sci. 469 (2019) 135–145.

[74] C. Rémazeilles, P. Refait, Fe (II) hydroxycarbonate Fe2 (OH) 2CO3 (chukanovite) as iron corrosion product: Synthesis and study by Fourier Transform Infrared Spectroscopy, Polyhedron 28 (4) (2009) 749–756.

[75] D. Bairagi, V. Munukuti, P. Bhuyan, R. Saha, S. Mandal, Effect of spheroidized microstructure on the impact toughness and electrochemical performance of a high-carbon steel, Mater. Corros. 72 (5) (2021) 829–838.

[76] M. Gao, X. Pang, K. Gao, The growth mechanism of CO_2 corrosion product films, Corros. Sci. 53 (2) (2011) 557–568.

[77] J.C. Brice, J.C. Brice, The Growth of Crystals from Liquids, Vol. 12, North-Holland Publishing Company Amsterdam, 1973.

[78] G.A. Schmitt, N. Stradmann, Wettability of steel surfaces at CO_2 corrosion conditions. I. effect of surface active compounds in aqueous and hydrocarbon media, in: CORROSION 98, OnePetro, 1998.

[79] A. Abdal-Hay, A.S. Hamdy, J.H. Lim, Facile preparation of titanium dioxide micro/nanofibers and tubular structures by air jet spinning, Ceram. Int. 40 (10) (2014) 15403–15409.

[80] H. Wang, C. Yu, X. Gao, L. Du, H. Wang, Corrosion behavior of ferrite-pearlite steel exposed to H_2S/CO_2 environment, Int. J. Electrochem. Sci. 15 (2020) 6737–6747.

[81] R. Nyborg, A. Dugstad, Mesa corrosion attack in carbon steel and 0.5% chromium steel, in: CORROSION 98, OnePetro, 1998.

[82] J.L. Crolet, N. Thevenot, S. Nešić, Role of conductive corrosion products on the protectiveness of corrosion layers, in: CORROSION 96, OnePetro, 1996.

[83] J. Crolet, S. Olsen, W. Wilhelmsen, Influence of a layer of undissolved cementite on the rate of the CO_2 corrosion of carbon steel, Tech. rep., NACE International, Houston, TX (United States), 1994.

[84] J. Crolet, W. Wilhelmsen, S. Olsen, Observations of multiple steady states in the CO_2 corrosion of carbon steel, Revue de Métallurgie 92 (1995).

[85] S. Chan, J. Charles, Effect of carbon content on hydrogen occlusivity and embrittlement of ferrite–pearlite steels, Mater. Sci. Technol. 2 (9) (1986) 956–962.

[86] D. Burkle, R. De Motte, W. Taleb, A. Kleppe, T. Comyn, S. Vargas, A. Neville, R. Barker, In situ $SR-XRD$ study of $FeCO_3$ precipitation kinetics onto carbon steel in CO_2-containing environments: The influence of brine pH, Electrochim. Acta 255 (2017) 127–144.

[87] T. Tanupabrungsun, B. Brown, S. Nešić, Effect of pH on CO_2 corrosion of mild steel at elevated temperatures, in: CORROSION 2013, OnePetro, 2013.

[88] M. Kermani, A. Morshed, Carbon dioxide corrosion in oil and gas production compendium, Corrosion 59 (08) (2003).

[89] W. Li, B. Brown, D. Young, S. Nešić, Investigation of pseudo-passivation of mild steel in CO_2 corrosion, Corrosion 70 (3) (2014) 294–302.

[90] H. Ma, X. Cheng, S. Chen, C. Wang, J. Zhang, H. Yang, An ac impedance study of the anodic dissolution of iron in sulfuric acid solutions containing hydrogen sulfide, J. Electroanal. Soc. 451 (1–2) (1998) 11–17.

[91] X. Cheng, H. Ma, J. Zhang, X. Chen, S. Chen, H. Yang, Corrosion of iron in acid solutions with hydrogen sulfide, Corrosion 54 (5) (1998) 369–376.

[92] H. Ma, X. Cheng, S. Chen, G. Li, X. Chen, S. Lei, H. Yang, Theoretical interpretation on impedance spectra for anodic iron dissolution in acidic solutions containing hydrogen sulfide, Corrosion 54 (8) (1998) 634–640.

[93] D. Shoesmith, P. Taylor, M. Bailey, B. Ikeda, Electrochemical behaviour of iron in alkaline sulphide solutions, Electrochim. Acta 23 (9) (1978) 903–916.

[94] B.D. Craig, The nature of iron sulfides formed on steel in an H_2S-O_2 environment, Corrosion 35 (3) (1979) 136–138.

[95] Y.-S. Choi, S. Nešić, S. Ling, Effect of H_2S on the CO_2 corrosion of carbon steel in acidic solutions, Electrochim. Acta 56 (4) (2011) 1752–1760.

[96] M. Lucio-Garcia, J. Gonzalez-Rodriguez, M. Casales, L. Martinez, J. Chacon-Nava, M. Neri-Flores, A. Martinez-Villafañe, Effect of heat treatment on H_2S corrosion of a micro-alloyed $C-Mn$ steel, Corros. Sci. 51 (10) (2009) 2380–2386.

[97] H. Ma, X. Cheng, G. Li, S. Chen, Z. Quan, S. Zhao, L. Niu, The influence of hydrogen sulfide on corrosion of iron under different conditions, Corros. Sci. 42 (10) (2000) 1669–1683.

[98] K. Videm, J. Kvarekvål, Corrosion of carbon steel in carbon dioxide-saturated solutions containing small amounts of hydrogen sulfide, Corrosion 51 (04) (1995).

[99] D.W. Shoesmith, P. Taylor, M.G. Bailey, D.G. Owen, The formation of ferrous monosulfide polymorphs during the corrosion of iron by aqueous hydrogen sulfide at 21 C, J. Electrochem. Soc. 127 (5) (1980) 1007.

[100] P. Marcus, E. Protopopoff, Potential-pH diagrams for adsorbed species: Application to sulfur adsorbed on iron in water at 25 and 300 C, J. Electrochem. Soc. 137 (9) (1990) 2709.

[101] Y. Zheng, J. Ning, B. Brown, S. Nešić, Electrochemical model of mild steel corrosion in a mixed H_2S/CO_2 aqueous environment in the absence of protective corrosion product layers, Corrosion 71 (3) (2015) 316–325.

[102] M.J. Cancio, M.L. Latino, T.E. Perez, Corrosion and hydrogen insertion in $UNS\ G41300$ steels in brine acid solutions saturated with hydrogen sulfide, in: CORROSION 2012, OnePetro, 2012.

[103] S.N. Smith, J.L. Pacheco, Prediction of corrosion in slightly sour environments, in: CORROSION 2002, OnePetro, 2002.

[104] W. Sun, S. Nešić, A mechanistic model of H_2S corrosion of mild steel, in: CORROSION 2007, OnePetro, 2007.

[105] E. Wallaert, T. Depover, I. De Graeve, K. Verbeken, FeS Corrosion products formation and hydrogen uptake in a sour environment for quenched & tempered steel, Metals 8 (1) (2018) 62.

[106] S.N. Smith, Current understanding of corrosion mechanisms due to H_2S in oil and gas production environments, in: CORROSION 2015, OnePetro, 2015.

[107] F. Pessu, Y. Hua, R. Barker, A. Neville, A study of the pitting and uniform corrosion characteristics of $X65$ carbon steel in different H_2S-CO_2-containing environments, Corrosion 74 (8) (2018) 886–902.

[108] B. Brown, D. Young, S. Nešić, Localized corrosion in an H_2S/CO_2 environment, in: The 17th International Corrosion Congress, NACE International, Houston, TX, 2009.

[109] M.D. Bonaventura, B. Brown, S. Nešić, M. Singer, Effect of flow and steel microstructure on the formation of iron carbonate, Corrosion 75 (10) (2019) 1183–1193.

[110] Z. Yin, L. Liu, Y. Wang, T. Yang, Y. Chen, Study on iron sulphide inhibition and corrosion of $80S$ and $110SS$ steels in acid solutions containing H_2S and CO_2, Int. J. Electrochem. Sci. 15 (2020) 10825–10843.

[111] P. Taylor, T. Rummery, D. Owen, Reactions of iron monosulfide solids with aqueous hydrogen sulfide up to 160 C, J. Inorg. Nucl. Chem. 41 (12) (1979) 1683–1687.

[112] A. Wikjord, T. Rummery, F. Doern, Crystallization of pyrite from deoxygenated aqueous sulfide solutions at elevated temperature and pressure, Canadian Mineral. 14 (4) (1976) 571–573.

[113] A. Wikjord, T. Rummery, F. Doern, D. Owen, Corrosion and deposition during the exposure of carbon steel to hydrogen sulphide-water solutions, Corros. Sci. 20 (5) (1980) 651–671.

[114] J. Ning, Y. Zheng, B. Brown, D. Young, S. Nešić, The role of pyrite in localized H_2S corrosion of mild steel, in: CORROSION 2017, OnePetro, 2017.

[115] D. Rickard, Kinetics of pyrite formation by the H_2S oxidation of iron (II) monosulfide in aqueous solutions between 25 C and 125 C: The rate equation, Geochim. Cosmochim. Acta 61 (1) (1997) 115–134.

[116] P. Bai, H. Zhao, S. Zheng, C. Chen, Initiation and developmental stages of steel corrosion in wet H_2S environments, Corros. Sci. 93 (2015) 109–119.